bioRxiv preprint doi: https://doi.org/10.1101/2020.07.10.197509; this version posted July 11, 2020. The copyright holder for this preprint (which was not certified by peer review) is the author/funder, who has granted bioRxiv a license to display the preprint in perpetuity. It is made available under a CC-BY-NC-ND 4.0 International license.
Manuscript submitted to *Cortex*

Cortical propagation as a biomarker for recovery after stroke

Gloria Cecchini[1,2†], **Alessandro Scaglione**[1,3†], **Anna Letizia Allegra Mascaro**[3,4†], **Curzio Checcucci**[1,3], **Emilia Conti**[1,3], **Ihusan Adam**[1,2,5], **Duccio Fanelli**[1,2,6], **Roberto Livi**[1,2,6], **Francesco Saverio Pavone**[1,3], **Thomas Kreuz**[7]

***For correspondence:** gloria.cecchini@unifi.it (Gloria Cecchini); thomas.kreuz@cnr.it (Thomas Kreuz)

[†]These authors contributed equally to this work

[1]Department of Physics and Astronomy, University of Florence, Sesto Fiorentino, Italy; [2]CSDC, University of Florence, Sesto Fiorentino, Italy; [3]European Laboratory for Non-linear Spectroscopy, University of Florence, Sesto Fiorentino, Italy; [4]Neuroscience Institute, National Research Council, Pisa, Italy; [5]Department of Information Engineering, University of Florence, Sesto Fiorentino, Italy; [6]INFN, Florence Section, Sesto Fiorentino, Italy; [7]Institute for Complex Systems (ISC), National Research Council (CNR), Sesto Fiorentino, Italy

Abstract

Stroke is a debilitating condition which affects millions of people worldwide. The development of improved rehabilitation paradigms rests on finding biomarkers suitable for tracking functional damage and recovery. We perform a detailed spatiotemporal analysis of wide-field calcium images from mice during longitudinal motor training before and after focal stroke induction. We define three indicators that characterise the duration, the angle of propagation and the smoothness of global movement-evoked activation patterns. During acute stroke we observe an increase in global event duration and a decrease in smoothness over the ipsilesional hemisphere. For both rehabilitation via motor training alone and combined with pharmacological therapy, we find clear signs of recovery, but surprisingly, cortical propagation in double treated mice with generalised recovery is even faster and smoother than before stroke. Our propagation-based biomarkers deliver unforeseen insight into brain mechanisms underlying motor recovery and thus pave the way towards a more targeted post-stroke therapy.

Introduction

Stroke is a severe disease that alters cortical processing producing long lasting motor or cognitive deficits. Treatments generally include motor rehabilitation, pharmacological therapies, brain stimulation, or combinations of them (***Stinear et al., 2020***). However, the functional outcome, measured as behavioural recovery, depends on multiple factors such as age, lesion size and type, edema formation or inflammation and is hardly predictable (***Burke Quinlan et al., 2015***; ***Prabhakaran et al., 2008***). One way to track recovery after stroke is by monitoring cortical activity, which is known to undergo drastic changes that have been tightly linked to structural alterations (***Carter et al., 2012***; ***van Meer et al., 2012***; ***Allegra Mascaro et al., 2019***). Previous studies have reported that stroke produces global widespread alterations in cortical activity as measured by changes in resting state functional connectivity or cortical excitability. On the one hand, electrophysiological studies have shown that stroke and recovery modulate both resting state and stimulus evoked cortical oscillations in motor areas (***Chen et al., 2017***; ***Cassidy et al., 2020***). On the other hand, neuroimaging studies have shown that stroke alters the resting state functional connectivity, for example it

bioRxiv preprint doi: https://doi.org/10.1101/2020.07.10.197509; this version posted July 11, 2020. The copyright holder for this preprint (which was not certified by peer review) is the author/funder, who has granted bioRxiv a license to display the preprint in perpetuity. It is made available under a CC-BY-NC-ND 4.0 International license.
Manuscript submitted to eLife

reduces the interhemispheric correlations between motor networks, and these changes correlate with behavioural deficits (***Carter et al., 2010***; ***van Meer et al., 2010***). Furthermore these changes in resting state functional connectivity can be used to discriminate subjects with behavioural deficits (***Rehme et al., 2015***). This supports the idea that monitoring how cortical activity evolves over time could be used to track recovery after stroke and it could represent a powerful tool to evaluate the efficacy of stroke treatments or better yet could lead to biomarkers of functional recovery.

Advancements in neural imaging combined with genetically encoded calcium indicators allow to monitor neural activity over almost the entire cortical mantle with high spatial resolution on a sub-second temporal scale (***Chen et al., 2013***; ***Harrison et al., 2013***; ***Vanni and Murphy, 2014***; ***Carandini et al., 2015***). Using these tools it has been shown that the neural activity of animals during a behavioural task is characterised by cortex-wide global activation patterns (***Allen et al., 2017***) and these patterns are shaped by learning across sessions (***Makino et al., 2017***). In the context of stroke calcium imaging has been used to demonstrate that stroke profoundly affects resting state functional connectivity (***Balbi et al., 2018***) and leads to sensorimotor remapping of the peri-infarct area (***Harrison et al., 2013***). Furthermore, in a recent study, we have shown that movement-related activation maps are different for stroke therapy associated with functional recovery (***Allegra Mascaro et al., 2019***). Therefore neural activity as measured by calcium imaging could be used as an indicator of cortical remapping, of redistribution of functional connectivity among spared regions and could be directly associated with behavioural recovery.

Here, we propose that damage and functional recovery can be tracked by monitoring the spatiotemporal properties of movement-evoked widespread activation patterns or global events. In particular, we use our recently proposed SPIKE-order analysis (***Kreuz et al., 2017***) to identify global events and to sort the participating regions from first to last (or leader to follower). In addition, to characterise the spatiotemporal properties of each individual global event, we extend this method and define three propagation indicators: duration, angle and smoothness, i.e. how ordered and consistent is the direction of the propagation.

First, we provide a characterisation of global events in healthy controls. We show that these events are mostly associated with the exertion of force and their duration and direction are modulated by different behavioural events. Then, to understand the impact of stroke on the global events we quantify the three propagation indicators in a group of acute stroke subjects. We provide evidences that acute stroke alters the propagation patterns by increasing the duration while decreasing the smoothness of the global events. Finally, to show that global events propagation patterns can be used to track recovery, we quantify the propagation indicators on two groups of subjects with different therapies; the first, robot, with motor training alone, and the second, rehab, with motor training combined with pharmacological therapy. We show that both treatments reverse the impact of stroke with the combined treatment, the only rehabilitative therapy previously associated with generalised recovery, characterised by the shortest duration and the highest smoothness among all different groups.

Methods

Experimental set-up and data collection

In this Section we provide a short overview of the data and the methods we used to analyse them. For more technical details please refer to the Section "Materials and Methods".

The aim of this study was to investigate changing propagation patterns during motor recovery from functional deficits caused by the induction of a focal stroke via a photothrombotic lesion. For this purpose, we analysed calcium imaging signals recorded from 17 mice during two long-term robot-assisted rehabilitation programs, one based on motor training alone and one combined with transient pharmacological inactivation of controlesional activity.

A schematic representation of the robotic system, the M-Platform (***Spalletti et al., 2014***; ***Pasquini et al., 2018***), is shown in Figure 1a. This system uses passively actuated contralesional forelimb ex-

bioRxiv preprint doi: https://doi.org/10.1101/2020.07.10.197509; this version posted July 11, 2020. The copyright holder for this preprint (which was not certified by peer review) is the author/funder, who has granted bioRxiv a license to display the preprint in perpetuity. It is made available under a CC-BY-NC-ND 4.0 International license.
Manuscript submitted to eLife

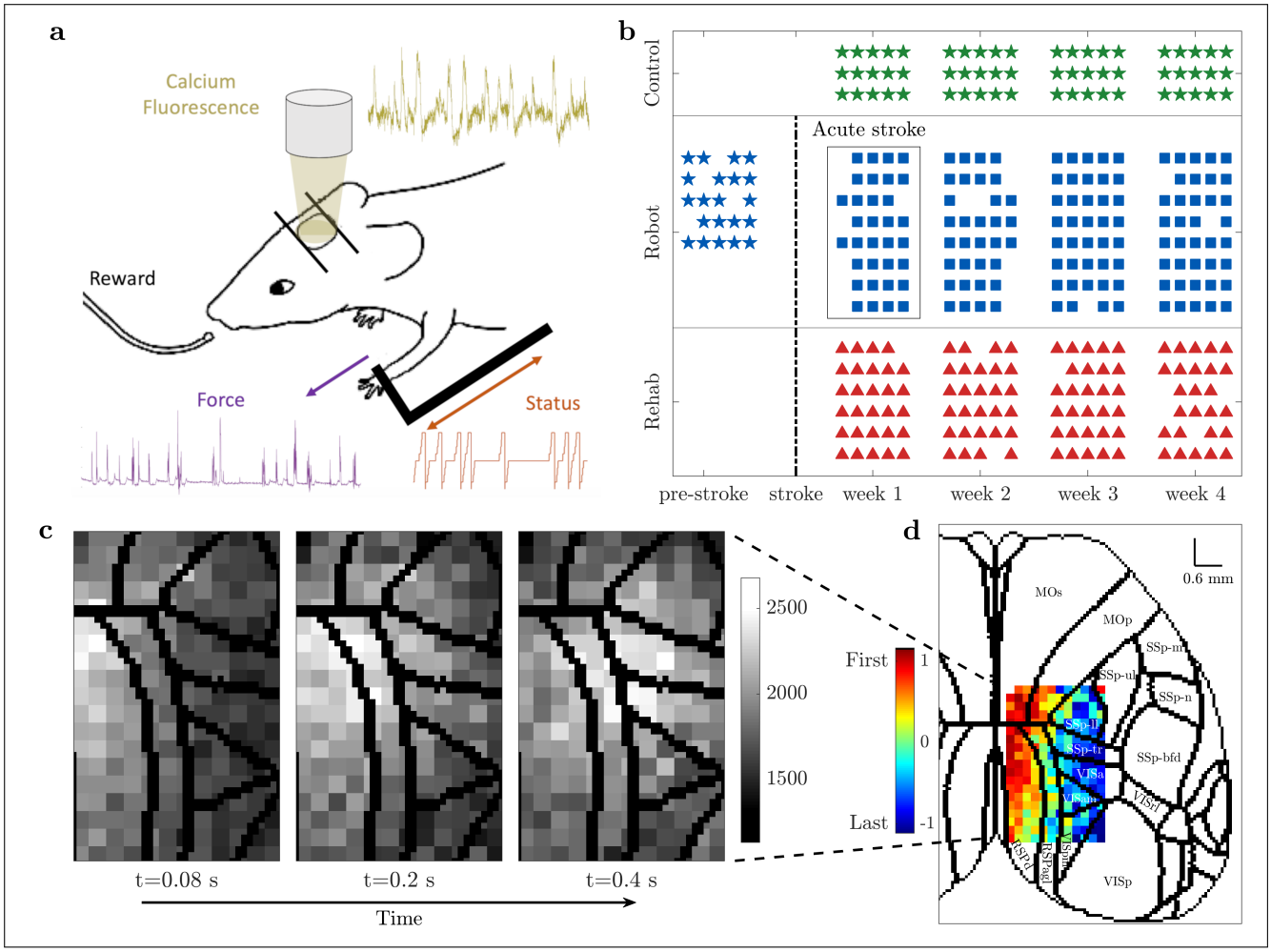

Figure 1. Experimental set-up and data collection. **(a)** Motor-training of mice was performed on the M-Platform, which uses a movable robotic slide for a retraction movement of the left forelimb. Motor activity was monitored via the discrete status of the slide (orange) and the force applied by the mouse to the slide (purple). Meanwhile, the cortical activity (yellow) was recorded using wide-field calcium imaging. **(b)** The control (green) and rehab (red) group performed 4 weeks of daily training; for the robot (blue) group we additionally recorded 1 week before stroke induction (typically 5 sessions per week). Star symbols refer to the healthy condition, while the two different types of rehabilitation, robot and rehab, are represented by squares and triangles, respectively. **(c)** Calcium imaging sequence (here 12 x 19 pixels) of cortical activation, superimposed on contours of brain regions according to the standard atlas. **(d)** Propagation pattern, from leader (red) to follower (blue), of the event depicted in (c).

Figure 1–video 1. Movie depicting the propagation of activity during the training cycle shown in Figure 1c. For caption see end of Appendix.

Figure 1–Figure supplement 1. Standard atlas of brain regions.

Figure 1–Figure supplement 2. Brain regions acronyms.

tension on a slide to trigger active retraction movements that were subsequently rewarded (up to 15 cycles per recording session). The effect of the motor activity was monitored via the discrete status of the slide and by recording the force the mice applied to the slide. As a measure of the neural activity itself we performed wide-field calcium imaging over the affected hemisphere, from the somatosensory to the visual areas. Selecting a region of interest of 2.16 x 3.78 mm and spatially downsampling by a factor 3 resulted in calcium images of 12 x 21 (or sometimes 12 x 19) pixels of size 180 μm. These are the signals that we analyze.

The 17 mice were divided into three groups: control (3 mice), robot (8 mice) and rehab (6 mice). The healthy controls had no stroke induced but still received the same motor training as the other mice (4 weeks on the M-Platform). Both robot and rehab mice underwent physical rehabilitation on the M-platform for 4 weeks starting 5 days after injury.

For rehab mice in addition a pharmacological inactivation of the primary motor cortex in the

bioRxiv preprint doi: https://doi.org/10.1101/2020.07.10.197509; this version posted July 11, 2020. The copyright holder for this preprint (which was not certified by peer review) is the author/funder, who has granted bioRxiv a license to display the preprint in perpetuity. It is made available under a CC-BY-NC-ND 4.0 International license.

contralesional hemisphere was carried out in order to counterbalance the hyperexcitability of the healthy hemisphere. The recording schedule for all three groups is shown in Figure 1b. Apart from the data acquisition during the shared training regime, 5 out of 8 robot mice were also recorded for one week before the stroke (pre-stroke condition).

Two weeks before the stroke, five mice belonging to the robot group have been trained for 5 days (pre-stroke condition), Figure 1b. We have tested whether the pre-stroke condition shows any statistical difference with the first week of recordings of the control group. As could be expected, the pre-stroke condition presents the same behaviour as the control group, both qualitatively and quantitatively.

Figure 1c displays a sequence of snapshots of the calcium activity over time. The three images illustrate one pull of the slide by the affected forelimb of a control mouse, from the activation of the average calcium activity (left) via its maximum (middle) to its tail end (right). The Supplementary Material contains a movie that covers all 36 frames for this one training cycle.

The central method of this study was a mapping of this sequence of snapshots into the propagation pattern shown in Figure 1d. In this matrix the order of activation of the individual pixels was color-coded from red (earliest) to blue (latest). We superimposed this order matrix on the standard atlas of brain regions (***Lein et al., 2007***) which illustrates that the recording area covers the primary motor area M1 (the location of the lesion), the primary somatosensory area, and the primary visual cortex, as well as the retrosplenial cortex.

Event identification, propagation analysis, and definition of three propagation indicators: duration, angle, and smoothness

Here we explain our use of the SPIKE-order framework (***Kreuz et al., 2017***) to identify global events and assess the propagation of activation within these events (compare Figure 1d). In particular, we focus again on one individual global event to illustrate how we characterise the detailed activation patterns with three propagation indicators: **duration**, **angle**, and **smoothness**.

In Figure 2 we show the activity during a complete recording session of one mouse. Figure 2a depicts the status, a discrete codification of the current phase of the passive extension and active retraction cycle, e.g. position of the slide and acoustic go and reward cues. Most relevant here are the marked times of the pull completions which typically correspond to peaks in the force applied to the slide (Figure 2b, force events are marked at threshold crossings) but already a quick look at the event numbers shows that the mapping is not perfect. Indeed there are typically more force events than rewarded pull completions (20 force versus 13 status events in this case). The same peaks, and some more, are also present in the calcium signal computed by averaging the fluorescence signal over all pixels (Figure 2c, here 23 calcium events are marked at threshold crossings).

In the next step we looked at all 19 x 12 = 228 individual pixels but here we do not show all the traces but just small time markers denoting the time of their threshold crossings (Figure 2d). This is very similar to a rasterplot showing in each row the spike train of one individual neuron and accordingly we here follow this terminology and call the threshold crossings of individual pixels 'spikes'. The first thing to notice is that while there are a few spikes in the background (in black), by far most of the spikes are part of global events (in color) matching the peaks in the average calcium activity shown right above. To automatically identify these global events and sort the spikes within these events from leader to follower we used the SPIKE-order framework proposed in (***Kreuz et al., 2017***).

After some initial denoising we first used an adaptive coincidence detector (***Quian Quiroga et al., 2002***) to pair spikes such that each spike is matched with at most one spike in each of the other pixels. By means of the symmetric and multivariate measure SPIKE-Synchronization (***Kreuz et al., 2015***) we filtered out all spikes which were not coincident with spikes in at least three quarters of the other spike trains. To the global events that remained we applied the asymmetric SPIKE-order indicator (***Kreuz et al., 2017***) which quantifies the leader-follower relationship between pairs of spikes. For each event the SPIKE-order is then color-coded from leader (red) to follower (blue).

bioRxiv preprint doi: https://doi.org/10.1101/2020.07.10.197509; this version posted July 11, 2020. The copyright holder for this preprint (which was not certified by peer review) is the author/funder, who has granted bioRxiv a license to display the preprint in perpetuity. It is made available under a CC-BY-NC-ND 4.0 International license.
Manuscript submitted to eLife

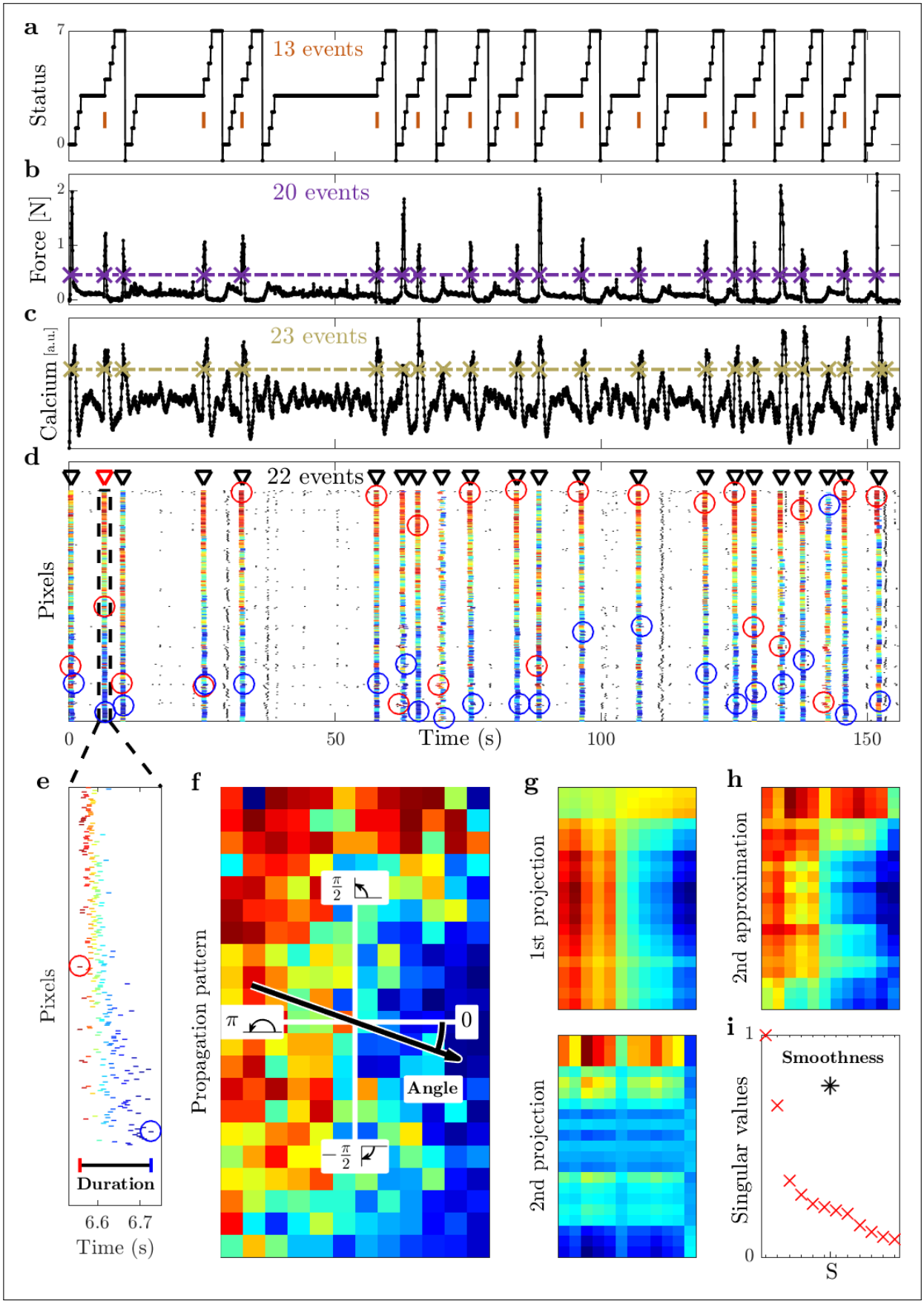

Figure 2. Event identification, propagation analysis, and definition of three propagation indicators: duration, angle, and smoothness.
Figure 2 continued on next page

bioRxiv preprint doi: https://doi.org/10.1101/2020.07.10.197509; this version posted July 11, 2020. The copyright holder for this preprint (which was not certified by peer review) is the author/funder, who has granted bioRxiv a license to display the preprint in perpetuity. It is made available under aCC-BY-NC-ND 4.0 International license.
Manuscript submitted to eLife

Figure 2 continued
(a) Status of the robotic slide. The longer horizontal plateaus at status 3 correspond to the time interval during which the mouse is allowed to retract the slide. The orange bars refer to the time when the pull is completed and the mouse receives its reward. **(b)** Force applied by the mouse during the retraction movement. **(c)** Average calcium signal over all pixels. The purple and yellow dashed lines below refer to the threshold used to identify the force and global calcium events, respectively. **(d)** Raster plot obtained from the threshold crossings of individual pixels versus time. Triangle indicators show the global events identified during this session, and the red triangle with dashed box marks the event analyzed in the remaining panels below. The first (last) spike of each global event is marked by a red (blue) circle. Within each subplot (a)-(d) we state the number of the respective events / threshold crossings. **(e)** Zoom of this selected event. The **duration** is defined as the interval from the first to the last spike within the event. **(f)** The propagation matrix is obtained by projecting the relative order of these threshold crossings onto the 2D-recording plane. By means of singular value decomposition (SVD) we obtain the **angle** of the propagation, defined relative to the horizontal axis. **(g)** First and second approximations of the propagation matrix and **(h)** second order approximation as their weighted sum (cumulative). **(i)** Singular values (red) vs. order of approximation. The **smoothness** (black asterisk) measures the quality of the approximation.

Finally, we used the scalar Synfire Indicator (***Kreuz et al., 2017***) to also sort the spike trains in the rasterplot from overall leader to overall follower. Since the sorting takes into account all global events, the first spike trains contain more leading spikes (red) and the last spike trains more trailing spikes (blue).

In Figure 2e we zoom in on the fourth global event of the rasterplot. Here we define the first propagation indicator, the event **duration**, as the time from the first to the last spike of this event. The propagation matrix of this specific event, obtained by projecting the colour-coded relative order of the spikes onto the pixels of the 2D-recording plane, is shown in Figure 2f. We then used singular value decomposition (SVD) to calculate the two remaining propagation indicators.

SVD (***Yanai et al., 2011***) searches for spatial patterns by decomposing the propagation matrix into three simple transformations: a rotation, a scaling along the rotated coordinate axes and a second rotation. The scaling is a diagonal matrix which contains along its diagonal the singular values of the propagation matrix. Backprojecting the (sorted) singular values one at a time resulted in various orders of approximations for the original propagation matrix. The first two such projections are displayed in Figure 2g and the second order approximation, their weighted sum, is shown in Figure 2h. From the weighted average of the mean gradients of these first two projections we calculated the second propagation indicator, the **angle** of the main propagation direction.

In Figure 2i we depict the (sorted) singular values (rescaled to the highest value) versus the order of the projection. We also show the value of the third propagation indicator, the **smoothness** S, which quantifies how well the approximation with only the first two singular values captures the full spatiotemporal pattern obtained by considering all singular values σ_i. Smoothness is defined as the relative weight of the first two projections, their sum divided by the sum of all singular values. This can be verified visually by comparing the second approximation (Figure 2h) with the original propagation matrix (Figure 2f).

A comparison of Figure 2d and Figure 2c clearly shows that all global events in the rasterplot can easily be matched with a peak in the average calcium trace, in fact, these are basically two equivalent ways to visualise a peak of global calcium activity. However, while the vast majority of global events are in close proximity of a peak in the force, not all of them are. This we can use to categorise the global events into two groups: Force (**F**) and non-Force (**nF**). Among the Force events we can distinguish two kinds of events, a few of them occur during the passive extension of the arm by the slide (Passive, **Pass**) but most of them do not, i.e., they occur during the active retraction phase (Active, **Act**). Finally, among those active events we can differentiate between movements which lead to a completion of the forelimb retraction and therefore are rewarded (Reward Pulling, **RP**) and movements which are not completed and thus not rewarded (non-Reward Pulling, **nRP**). The Reward Pulling events are the ones that correspond to the vertical markers in the status trace of Figure 2a.

The overall categorisation can be visualised by means of this branching structure:

bioRxiv preprint doi: https://doi.org/10.1101/2020.07.10.197509; this version posted July 11, 2020. The copyright holder for this preprint (which was not certified by peer review) is the author/funder, who has granted bioRxiv a license to display the preprint in perpetuity. It is made available under a CC-BY-NC-ND 4.0 International license.
Manuscript submitted to eLife

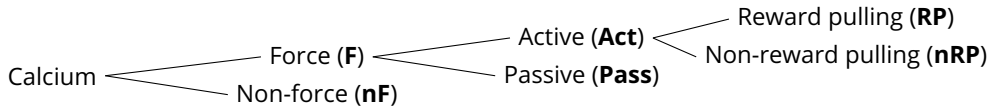

Results

In this study, we sought a biomarker for functional recovery after stroke in the neural activity propagation. To this aim, we used global event propagation analysis to investigate the spatiotemporal features of neuronal activation over the dorsal cortex. We compared the propagation patterns in healthy versus acute stroke and after treatment mice (control, robot, and rehab groups, compare Figure 1). We decided to investigate three main indicators (angle, duration, and smoothness of the propagation) to account for both spatial and temporal propagation characteristics (compare Figure 2). To identify common brain dynamics associated with similar behaviours, we have dealt with each type of event separately.

Global events are mostly associated with generation of voluntary movements in healthy mice

We first wondered if neuronal activation in awake mice involved a large region of the cortex and if these global events were related to specific classes of behavioural events in our experimental paradigm. The results in Figure 3 focus on the number of events and two of the three indicators introduced in Figure 2 (angle and smoothness) and they refer to one healthy mouse during all sessions (4 weeks, 5 days per week, see Figure 1b).

For this mouse, a total of 537 global events are identified, of these 492 (92%) are associated with force events (Figure 3a, see Table 1 for more details). Moreover, 356 (66%) of the selected global events are pulling events. Pulling the handle is a relatively easy task which allows even animals right after stroke to perform it; this is reflected by the fact that the majority of behavioural events are reward pulling events (277, 56%).

Three different example patterns with increasing smoothness and varying angle are depicted in panels (b-d). For low smoothness values, the identified propagation pattern looks random, thus not displaying a clear directionality (panel (b)), and therefore measures for angle and duration are less meaningful in those cases. On the other hand, high smoothness corresponds to clear patterns (panels (c-d) show two cases of high smoothness but orthogonal directionality). Panels (e-g) show scatter plots of smoothness against angle for different event types, together with the marginal histograms. While narrowing down the type of event does not reduce the whole range of values, the marginal distributions of the angle and smoothness converge to a peak distribution for the angle centred in 0.46, and to a distribution with mean 0.68 for the smoothness.

In summary, in healthy mice a large number of global events can be detected, and a vast majority of them are associated with application of force to the handle. The variety of the identified propagation patterns suggests a more in depth analysis of the propagation indicators across event types.

Cortical propagation features discriminate event types in healthy mice

In the previous section we established the presence of global events within the cortical activation during motor training. Here we characterised these events based on their behavioural condition. Then, we addressed if longitudinal motor training altered the propagation patterns. To this end, a detailed quantitative analysis of all three indicators (angle, smoothness and duration) was performed for three healthy mice along four weeks of motor training on the M-Platform (control group). Moreover, the dependency of these quantities was evaluated both over time and with respect to different event types (Figure 4).

bioRxiv preprint doi: https://doi.org/10.1101/2020.07.10.197509; this version posted July 11, 2020. The copyright holder for this preprint (which was not certified by peer review) is the author/funder, who has granted bioRxiv a license to display the preprint in perpetuity. It is made available under a CC-BY-NC-ND 4.0 International license.

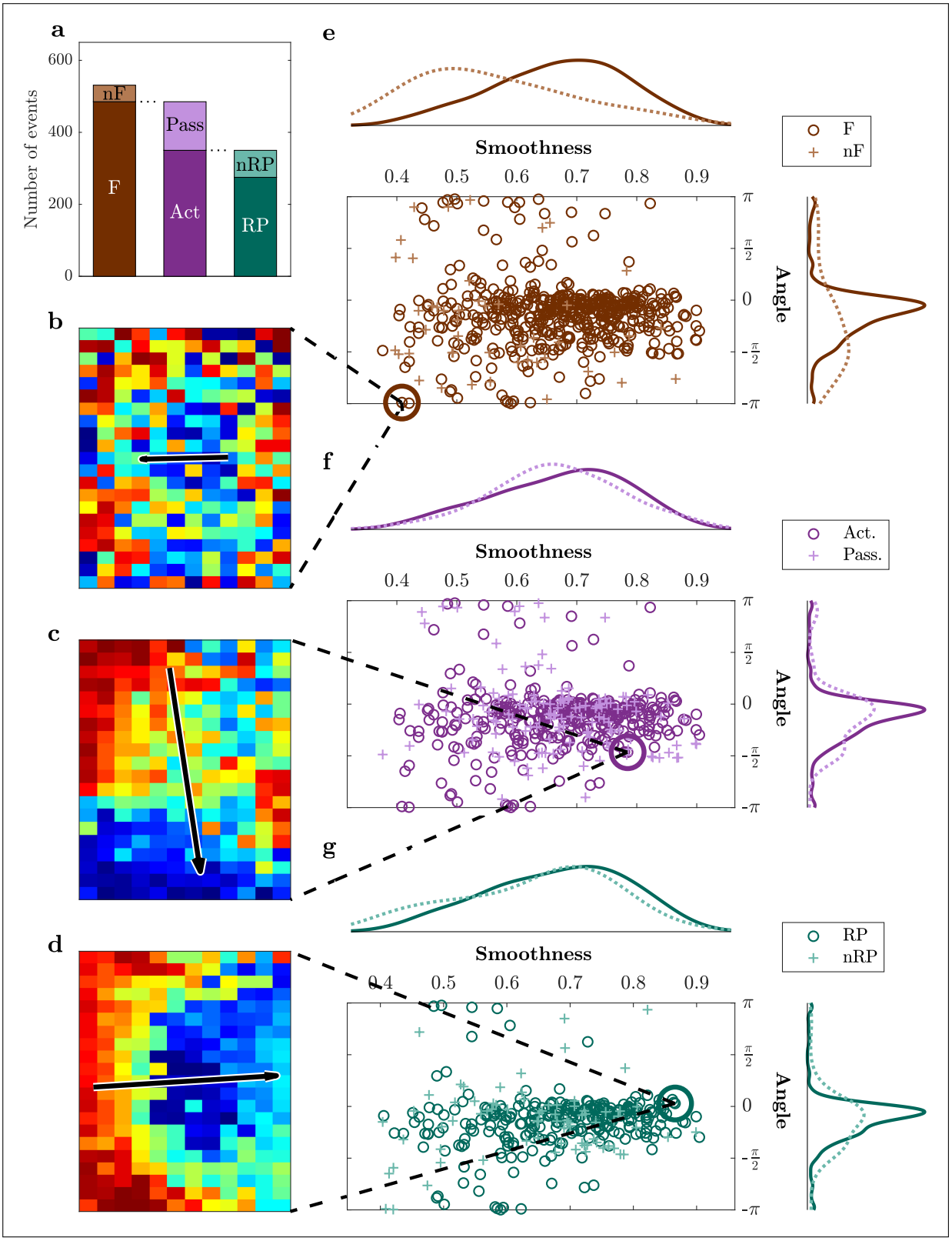

Figure 3. Propagation pattern varies across event types in healthy mice. **(a)** Classification of events. **(b-d)** Three different patterns with increasing smoothness and varying angle. Note that the length of the arrow is proportional to the smoothness. **(b)** Low smoothness identifies a poor propagation pattern without any proper directionality. **(c)** High smoothness identifies a clear pattern and corresponding directionality. **(d)** High smoothness and horizontal propagation in contrast with (b) low smoothness and opposite horizontal direction, and different from (c) which has still high smoothness, but an almost orthogonal angle of $-\pi/2$. **(e-g)** Scatter plots and histograms of smoothness and angle of propagation for all events. — Brown colours refer to force (F) and non-force (nF) events, active (Act) and passive (Pass) events are in purple, reward pulling (RP) and non-reward pulling (nRP) events in green. All plots include the events from all the sessions for one healthy mouse.

bioRxiv preprint doi: https://doi.org/10.1101/2020.07.10.197509; this version posted July 11, 2020. The copyright holder for this preprint (which was not certified by peer review) is the author/funder, who has granted bioRxiv a license to display the preprint in perpetuity. It is made available under a CC-BY-NC-ND 4.0 International license.
Manuscript submitted to bioRxiv

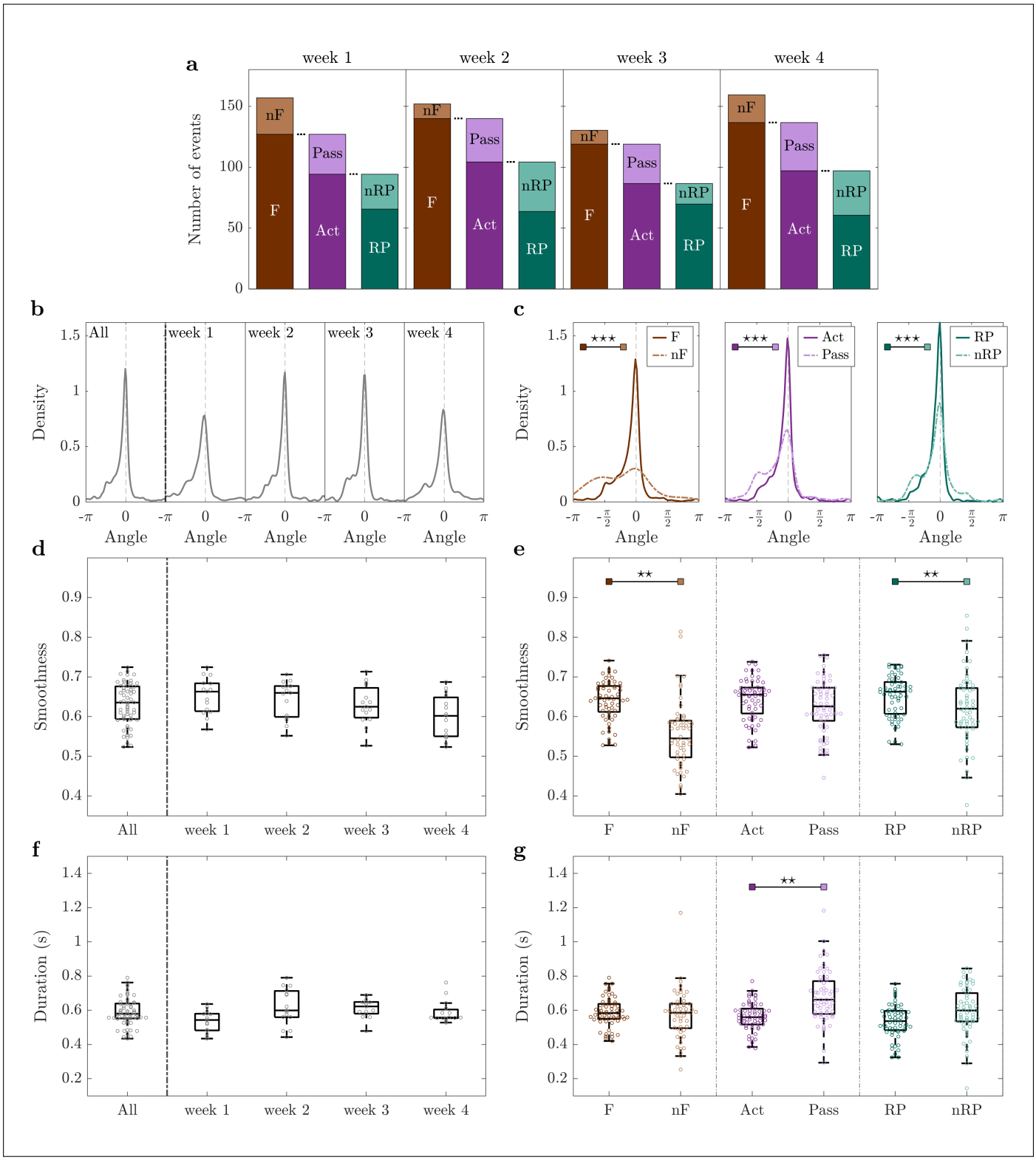

Figure 4. Cortical propagation features discriminate event types in healthy mice. **(a)** Mean number of events for all three mice per week, partitioned by type of event. **(b-c)** Narrowing down the type of event leads to more directed propagation patterns. **(d-e)** Smoothness discriminates force (F) and non-force (nF) events, and is preserved over weeks. **(f-g)** Event duration is a marker for discriminating active (Act) and passive (Pass) events, as well as reward pulling (RP) and non-reward pulling (nRP) events. — Angle and duration are weighted by smoothness. Markers in (d-g) refer to the average value per day. Within each box in (d-g), the central mark indicates the median, and the bottom and top edges of the box indicate the 25th and 75th percentiles, respectively. Control group n=3 mice. P-values of statistical tests in Table 2, "⋆" refers to difference in variance.

bioRxiv preprint doi: https://doi.org/10.1101/2020.07.10.197509; this version posted July 11, 2020. The copyright holder for this preprint (which was not certified by peer review) is the author/funder, who has granted bioRxiv a license to display the preprint in perpetuity. It is made available under a CC-BY-NC-ND 4.0 International license.

We first analysed if the occurrence of the global events was associated with the application of forces or if it was unrelated. The variation of the number of events divided by type is depicted in Figure 4a and it refers to the four weeks of recordings (compare to the first three rows (green stars) in Figure 1b). Most of these events occurred when the mouse applied a force to the handle (1568, corresponding to 87% of the total number of events). Furthermore, most of the force events (1147) occurred when the mouse was actively pulling the handle (73% of force events, 64% of the total), and 779 of those corresponded to reward pulling events (68% of active events, 43% of the total). Global events propagate along angles -0.3 ± 0.4 with a smoothness of 0.63 ± 0.03, and they last 0.59 ± 0.04 s, see subplot "All" of Figure 4b,d,f. The little variation in the angle (Figure 4b), smoothness (Figure 4d) and duration (Figure 4f) implies high coherence of the parameters of spatiotemporal propagation over weeks. This suggests that motor training alone does not change events number, duration, score or angle along weeks.

Results for angle, smoothness and duration were then analysed looking at specific event types. Figure 4c shows the distributions of the angle for the three consecutive subdivisions of the event types. The propagation becomes more directed when narrowing down the type of event. The difference between event types in the angle distribution reduces as well. Interestingly, also the bimodal nature of the distribution is attenuated. Specifically, the peak at $-\pi/2$ (see first plot in Figure 4c) is initially caused by non-force events, then within force events it stands out in the passive cases, finally it is predominant in the non-reward pulling events. This suggests that task-specific events, such as reward pulling, are characterised by consistent propagation patterns. The same argument can be made for the smoothness of the propagation; further specifying the type of event leads to smoother and smoother propagation patterns (Figure 4e) with the highest average smoothness being obtained for reward pulling events. They display also the shortest duration, on average, among all the other events (Figure 4g).

The patterns observed in healthy mice are characterised by different spatiotemporal features when comparing force and non-force events in terms of angle (p=10^{-10}) and smoothness (p=0.001) of propagation, and when comparing active and passive events in terms of angle (p=10^{-9}) and duration (p=0.002). Also between rewarded and non-rewarded pulls events the observed patterns display different characteristics when comparing angle (p=10^{-8}) and smoothness (p=0.001), see Figure 4c,e,g and Table 2.

In summary, in healthy mice there is a high coherence of the parameters of spatiotemporal propagation over weeks, suggesting that on a simple motor task alone does not change the angle, smoothness, and duration of events. Moreover, the investigated spatiotemporal propagation indicators discriminate between different event types when a specific characteristic is taken into account, i.e., force versus non-force, active versus passive, reward versus non-reward pulling.

Acute phase after stroke is characterised by an increase of event duration.

We pondered how the spatiotemporal propagation indicators were altered by cortical injury, and thus looked at the cortical activation events as associated to classes of behavioural events in the first week right after the stroke (called acute stroke). Moreover, we compared these results with the first week of recordings on healthy mice (Figure 5) which consists of the first week of recordings of the control group and the pre-stroke week in the robot group (see ***Figure 5–Figure Supplement 1*** for a comparison).

When looking at all events together, the angles distribution for the acute stroke group exhibits a flatter distribution and two secondary peaks in $-\pi/2$ and $\pi/2$, indicating the presence of a more heterogeneous pool of events (Figure 5a). Differences can be appreciated for the smoothness (p=0.007) and duration (p=0.003) even without further splitting the events into specific types. In particular, the smoothness decreases (Figure 5c) and the duration increases (Figure 5e) during the acute phase. Day by day variations are shown in Figure 5g-h. For both smoothness and duration, the difference of control and acute stroke groups is considerably larger for the first 3 days. Moreover, the difference in the event duration tends to diminish over days.

bioRxiv preprint doi: https://doi.org/10.1101/2020.07.10.197509; this version posted July 11, 2020. The copyright holder for this preprint (which was not certified by peer review) is the author/funder, who has granted bioRxiv a license to display the preprint in perpetuity. It is made available under a CC-BY-NC-ND 4.0 International license.

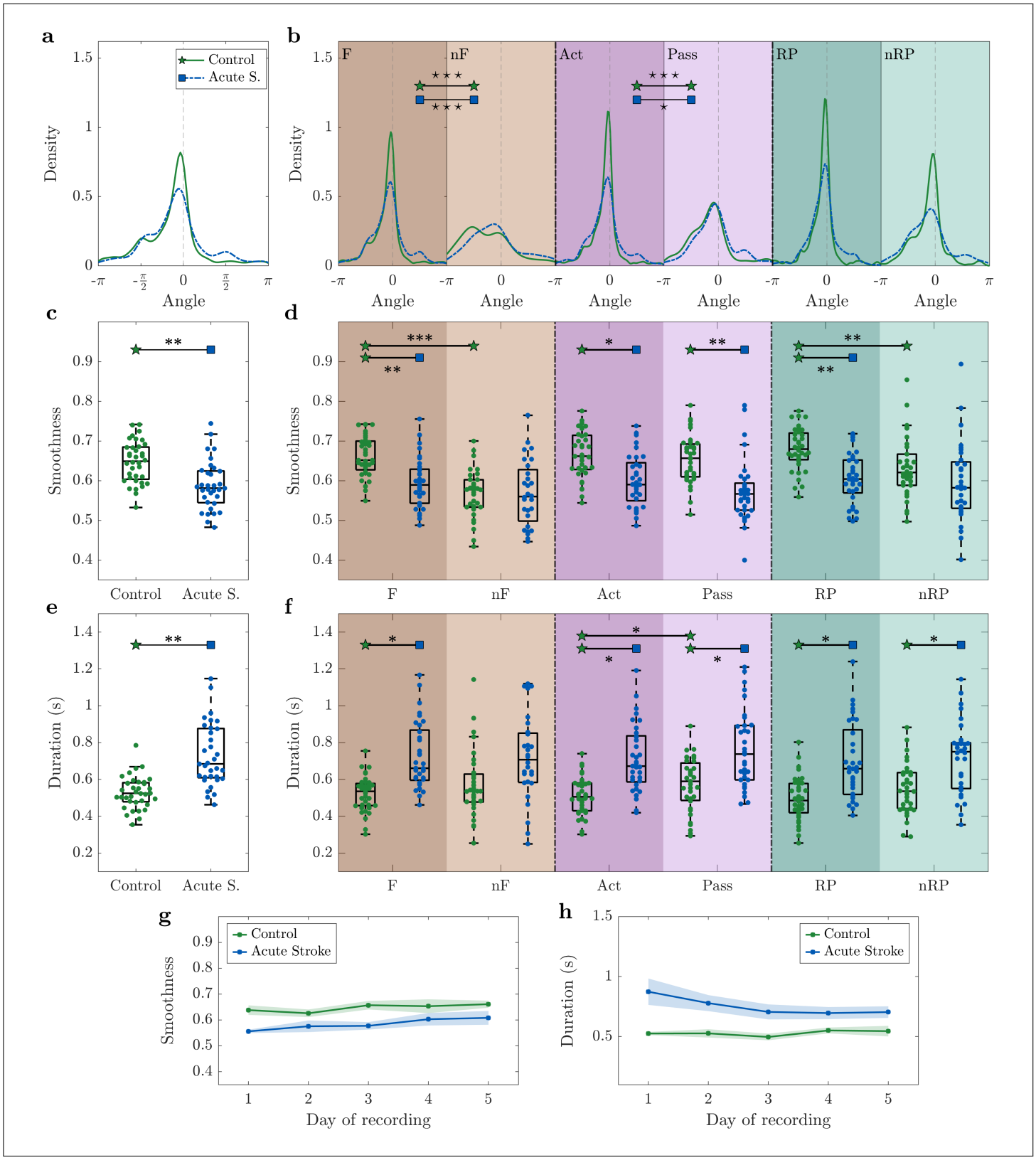

Figure 5. The acute phase (1 week after stroke) is characterised by an increase of the event duration. During the acute phase, **(a-b)** the direction of propagation is more spread, **(c-d)** smoothness is decreased, and **(e-f)** the event duration is increased. **(g)** While smoothness is higher for control mice, this difference tends to diminish over days. **(h)** Event duration is longer for stroke mice, attenuating day by day. — Angle and duration are weighted by smoothness. Markers in (c-h) refer to the average value per day. Within each box in (c-f), the central mark indicates the median, and the bottom and top edges of the box indicate the 25th and 75th percentiles, respectively. Shaded areas in (g-h) correspond to the confidence interval. Control n=8 mice, Acute Stroke n=8 mice. P-values of statistical tests in Table 3, "⋆" refers to difference in variance and "*" refers to difference in mean.

bioRxiv preprint doi: https://doi.org/10.1101/2020.07.10.197509; this version posted July 11, 2020. The copyright holder for this preprint (which was not certified by peer review) is the author/funder, who has granted bioRxiv a license to display the preprint in perpetuity. It is made available under a CC-BY-NC-ND 4.0 International license.
Manuscript submitted to eLife

Figure 5–Figure supplement 1. The pre-stroke condition presents the same behaviour as the control group.

When splitting the results into event types (Figure 5b,d,f), a common tendency for angle, smoothness and duration is that the stroke condition attenuates differences of the indicators between event types. For the angle (Figure 5b), the dissimilarities in the control group between event types are preserved in the acute stroke condition (F-nF and Act-Pass, control $p<0.001$ and robot $p<0.05$). For both smoothness and duration (Figure 5d,f), while the control group presents significant variations changing the type of event (F-nF $p=10^{-10}$ and RP-nRP $p=0.008$ for smoothness, and Act-Pass $p=0.04$ for duration), the acute stroke group is characterised by smaller fluctuations in the mean value (F-nF $p=0.082$ and RP-nRP $p=0.51$ for smoothness, and Act-Pass $p=0.059$ for duration). Regarding the smoothness (Figure 5d), a significant difference in mean between healthy and stroke mice can be appreciated for force (F, $p=0.004$), active (Act, $p=0.01$), passive (Pass, $p=0.002$), and reward pulling (RP, $p=0.005$) events. For the duration (Figure 5f), significant differences can be found in the same events types as for smoothness ($p=0.026$, 0.034, 0.035, 0.014) with the addition to the not reward pull (nRP, $p=0.028$) events. A more detailed description of the p-values of the test is presented in Table 3.

Altogether, our three spatiotemporal propagation indicators are able to distinguish between healthy and stroke mice. The acute phase after stroke leads to more heterogeneous events characterised by flattened distributions of the angle, lower smoothness, and longer duration. Moreover, in contrast to the healthy condition, cortical propagation features do not discriminate event types in the acute stroke condition.

Combined rehabilitative treatment induces higher smoothness and shorter duration of cortical propagation patterns

We wondered if the combined treatment leading to generalised recovery (as shown in (***Spalletti et al., 2017***)) was associated with a specific fingerprint of cortical activation patterns. We hypothesised that rehabilitative treatments may alter the spatiotemporal propagation patterns, and in particular reverse the trend observed in the acute stroke phase. We therefore compared the spatiotemporal propagation indicators in animals treated with motor training alone (robot group) or in combination with pharmacological inactivation of the homotopic cortex (rehab group). Finally, by comparing treated (robot and rehab) with healthy mice (control group), we evaluated if propagation features were restored to pre-stroke levels or if the treated condition ended in a new state (Figure 6). To this end, in this section we analysed data belonging to control, robot, and rehab groups starting from the second week of recording up to one month after stroke.

The most striking result emerging from this analysis is that the rehab group is greatly separated from both the control and the robot group for all three propagation indicators. To find differences between groups in the angle distribution it is not sufficient to look at all events together (Figure 6a), but instead it is necessary to split the results into event types (Figure 6b). The rehab group is significantly different from both control and robot groups when considering force, active, passive, and reward pulling events. Interestingly, in the rehab group neither qualitative nor quantitative variations in the angle distribution across event types can be observed. More specifically, the distribution of the angles appears to be consistent for different event types.

The events of the rehab group display a greater smoothness compared to the control ($p=0.025$) and robot ($p=10^{-4}$) groups. The biggest difference can be observed for rehab versus robot group; it is significant not only for all events together ($p=10^{-4}$, Figure 6c) but also for each event type separately (all $p<0.01$, Figure 6d). Note that, as for the angle, the smoothness of the rehab group appears to be consistent when distinguishing different event types, meaning force, non-force, active, passive, reward and non-reward pulling events display the same average smoothness value.

Among all the characteristics investigated, the marker that distinguishes most clearly between the rehab group and control ($p=10^{-4}$) and robot ($p=10^{-6}$) groups is duration. The events of the

bioRxiv preprint doi: https://doi.org/10.1101/2020.07.10.197509; this version posted July 11, 2020. The copyright holder for this preprint (which was not certified by peer review) is the author/funder, who has granted bioRxiv a license to display the preprint in perpetuity. It is made available under a CC-BY-NC-ND 4.0 International license.

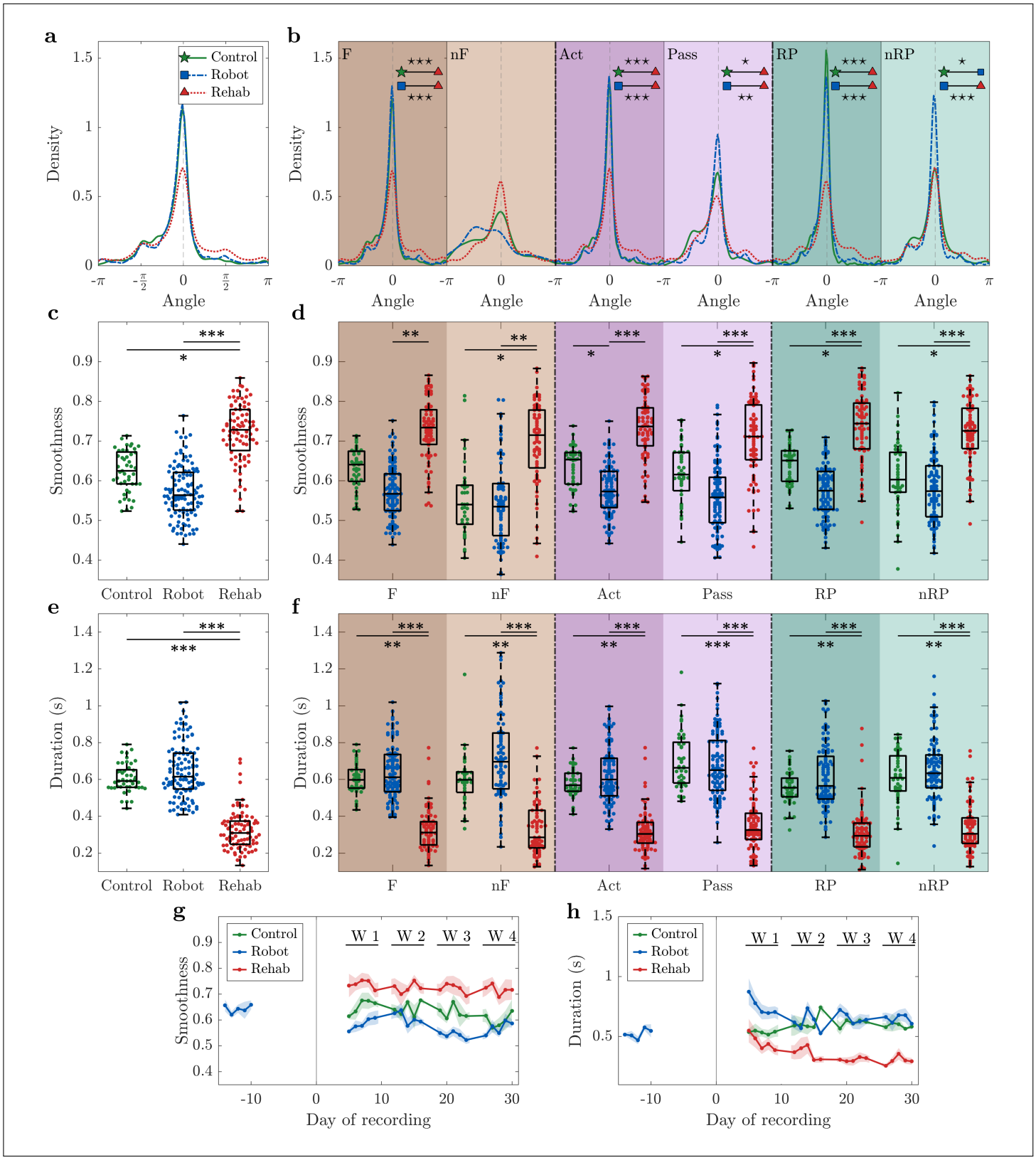

Figure 6. Rehab group is characterised by higher smoothness and shorter duration. **(a-b)** For the rehab group the distribution of the angles does not vary depending on the type of event. **(c-d)** For all types of event, the smoothness of the rehab group is higher than for the robot group. **(e-f)** For all types of event, rehab group events are the shortest. **(g)** Smoothness is always higher for the rehab group. **(h)** Event duration is always shorter for the rehab group. As expected, for both smoothness and duration the pre-stroke week of the robot group is quantitatively the same as the first week of the control group.

Figure 6 continued on next page

bioRxiv preprint doi: https://doi.org/10.1101/2020.07.10.197509; this version posted July 11, 2020. The copyright holder for this preprint (which was not certified by peer review) is the author/funder, who has granted bioRxiv a license to display the preprint in perpetuity. It is made available under a CC-BY-NC-ND 4.0 International license.
Manuscript submitted to eLife

Figure 6 continued
— Angle and duration are weighted by smoothness. Markers in (c-h) refer to the average value per day. Within each box in (c-f), the central mark indicates the median, and the bottom and top edges of the box indicate the 25th and 75th percentiles, respectively. Shaded areas in (g-h) correspond to the confidence interval. Control group n=3 mice, robot group n=8 mice, rehab group n=6 mice. P-values of statistical tests in Table 3, "⋆" refers to difference in variance and "*" refers to difference in mean.

Figure 6–Figure supplement 1. The robot group presents a non-stationary evolution over weeks and large variance of all three indicators.
Figure 6–Figure supplement 2. The rehab group shows high coherence of all three spatiotemporal indicators starting from the second week of training after stroke.

rehab group are shorter than for the control (all p<0.01) and robot (all p<0.001) groups (Figure 6e-f). Again, this statement applies to all events together (Figure 6e) as well as to each event type individually (Figure 6f). Also in this case, the duration of the rehab group appears to be consistent when looking at different event types. The complete list of the p-values of the test can be found in Table 4.

Figures 6g-h depict the trend over time of smoothness and duration. The control group shows a consistent trend, suggesting that motor training alone has no effect on either smoothness or duration, as already described in the previous sections for healthy mice (Figure 4). After the stroke, the robot group shows a significant variation: the smoothness is lower and the duration is longer. This variation decreases over time in both cases. While for the smoothness this difference seems to oscillate without stabilising, the duration reaches again values comparable to healthy mice already after the second week of training. Interestingly, the rehab group presents a behaviour qualitatively comparable to the control group, i.e., a consistent trend, but with very different values.

In summary, the rehab group is significantly different from both control and robot groups. In particular, it is characterised by higher smoothness and shorter duration. Differences between the rehab and the other two groups can be observed not only for all events together, but also for specific event types. Specifically, when looking at specific event types (force, non-force, active, passive, reward pull, non-reward pull) our three spatiotemporal propagation indicators are able to distinguish the rehab group from the control and robot groups.

Discussion

In this study we employed an improved version of our recently proposed SPIKE-order analysis (***Kreuz et al., 2017***) to sequences of wide-field fluorescent calcium images from the dorsal cortex of awake behaving mice. We defined three propagation indicators that characterise the duration, the angle of propagation and the smoothness of movement-evoked global events. This new way of quantifying variations in the spatiotemporal propagation patterns during longitudinal motor training allowed us to track damage and functional recovery following stroke.

We found that in healthy mice all three indicators of spatiotemporal propagation display a very high degree of consistency over time. For animals with acute stroke the propagation patterns of the global events are altered. The most prominent consequence is a large increase in global event duration and a decrease in smoothness over the ipsilesional hemisphere. We compared two different rehabilitation therapies, motor training alone and motor training combined with pharmacological therapy. While both reverse the effects observed during the acute phase, the combined treatment, promoting a generalised recovery, leads to a new functional efficacy, different from pre-stroke conditions, with very fast and smooth propagation patterns.

Comparison with existing methods

Comparing our approach with techniques previously applied in similar contexts, we first note that most analysis tools for wide-field optical images perform simple correlation and time lag analysis (Pearson correlation and phase synchrony), which are window- and not event-based (e.g. ***Haupt et al.*** (***2017***); ***Brier et al.*** (***2019***); ***Vanni et al.*** (***2017***)). Directionality is explored by using Granger causality in (***Mitra et al., 2018***), which is dependent on a priori selection of regions of interest (ROIs). Since commonly used analyses tools are based on averaged activity under resting state,

bioRxiv preprint doi: https://doi.org/10.1101/2020.07.10.197509; this version posted July 11, 2020. The copyright holder for this preprint (which was not certified by peer review) is the author/funder, who has granted bioRxiv a license to display the preprint in perpetuity. It is made available under a CC-BY-NC-ND 4.0 International license.

important information on single events is missing. This is especially important when considering motor evoked activity, which is directly associated with the execution of single movements (active forelimb pulling in our case). The detailed propagation analysis we showed here would not be possible with the widely used optical flow techniques (***Afrashteh et al., 2017***; ***Townsend and Gong, 2018***) which instead focus on velocity vector fields and their complex patterns (e.g. sources and sinks) but do not deal explicitly with temporal order. Our methods used here contain some similarities but also crucial differences with a very recent analysis performed on cortical slow waves in anaesthetised mice (***Celotto et al., 2020***). On the one hand, both algorithms apply exactly the same criteria of unicity and globality in the identification of the spatiotemporal patterns. On the other hand, the core of our global event detection is automated spike matching (via adaptive coincidence detection) while the wavehunt pipeline relies on an iterative procedure to cut the time series into distinctive waves. Apart from the different types of data, the two studies are also complementary in scope: while the focus of ***Celotto et al.*** (***2020***) lies on the excitability of the neuronal population, the dominant origin points and the velocity of the slow waves, we perform a thorough investigation of the spatial propagation pattern of each global event. Nevertheless, it would be very interesting to compare our SPIKE-order approach and their wavehunt pipeline in more detail and we will make this the topic of a future study.

Cortical propagation features in healthy mice

We first tested the discrimination capabilities of this approach for different classes of behavioural events and used it to characterise global events over most of the dorsal cortex. Results show that under our experimental paradigm, in all conditions, global events are occurring predominantly when the mouse is actively applying force during either active retraction or passive extension of the affected forelimb. Angle, duration and smoothness of the global events change with behavioural event type (e.g. if the event is associated with the application of force or not) in healthy subjects. This finding is in line with a recent study showing different propagation patterns across the cortex for mice engaged in a visual task depending on the type of the behavioural event (active vs passive, hit vs misses, ipsilesional vs controlesional) (***Steinmetz et al., 2019***).

None of the parameters of global cortical activation were significantly altered by daily training over four weeks, suggesting that the spatiotemporal propagation is not strongly correlated with the repeated performance of the forelimb pulling task. In our study, the duration of the propagation in global events is quite stable over the weeks. Recent literature shows that the cortical propagation changes over different learning phases (***Makino et al., 2017***). Makino and colleagues find that as learning progresses the activity across cortical regions became temporally more compressed, and its trial-by-trial variability decreased. As we showed in a previous paper (***Allegra Mascaro et al., 2019***), the active pulling task is very easily and rapidly learned by the mouse, so a possible learning effect might not be revealed.

The drastic change observed in the angle distribution of global events between force and non force events implies that activity propagates from medial to lateral regions. This is in accordance with previous findings based on space-frequency single value decomposition analysis showing that at the naive stage, the activity propagated from retrosplenial cortex in a radial direction (***Makino et al., 2017***). Also, the small hump in the angle distribution at $-\pi/2$ (panels b and c of Figure 4), indicative of rostro-caudal propagation, is reminiscent of the flow of activity from premotor cortex towards caudal regions emerging during learning in (***Makino et al., 2017***). The mediolateral propagation of the global events suggests the progressive involvement of the retrosplenial cortex during the exertion of the reward pull. Indeed, it has been previously reported that retrosplenial cortex is more correlated with sensory cortices during locomotion vs quiescence (***Clancy et al., 2019***) suggesting the presence of a network switch to allow the processing of sensory information during locomotion. In this view, the higher accumulation of angles at 0 degrees observed when comparing force vs non force events could represent the hallmark of such network switch. Interestingly, a similar propagation pattern has been observed applying optical flow analysis to calcium imaging

bioRxiv preprint doi: https://doi.org/10.1101/2020.07.10.197509; this version posted July 11, 2020. The copyright holder for this preprint (which was not certified by peer review) is the author/funder, who has granted bioRxiv a license to display the preprint in perpetuity. It is made available under a CC-BY-NC-ND 4.0 International license.
Manuscript submitted to eLife

over the same cortical areas when windowing cortical activity around hippocampal sharp wave ripples during sleep (***Karimi Abadchi et al., 2020***) and corresponds to one of the two major propagation patterns observed during slow wave sleep (***Greenberg et al., 2018***). Our findings extend these results to the awake condition during motor execution.

Acute phase after stroke

Stroke strongly affects the spatial propagation within the cortex during the execution of a pulling task. The analysis of spatiotemporal propagation patterns evoked by stimulation or voluntary movements represents a fundamental means to investigate functional remapping in order to better understand post stroke reorganisation. In our study, acute stroke is characterised by less coherent direction of the propagation, lower smoothness, and longer duration than healthy animals. Also, cortical propagation properties are very heterogeneous across global events and the differences between behavioural event types are lost.

In a previous work Murphy and collaborators (***Brown et al., 2009***), by applying intrinsic optical signal and fluorescence imaging, described modifications in spatiotemporal propagation elicited by sensory forelimb stimulation both in acute and chronic phase after stroke in the forelimb cortex. In agreement with Brown et al., who observed during the acute phase an increase of time to peak cortical signal evoked by sensory stimulation, our results revealed an increment of duration of motor-evoked cortical response, showing a delayed activation of cortical regions neighbouring the stroke core due to the damage. The comparison between these results reveals that though applying opposite approaches (i.e. bottom-up for sensory stimulation and top-down for motor task execution) a similar cortical response was observed. Moreover, an fMRI study in the acute phase by Dijkhuizen and colleagues (***Dijkhuizen et al., 2003***) showed that the stimulation of the unpaired forelimb induces a small response detected in the ipsilesional hemisphere in M1 and sFL cortex and in more distal regions both in rostral and caudal direction. A similar observation was made by Harrison and collaborators (***Harrison et al., 2013***) revealing that motor maps were more diffuse after motor-targeted stroke during sensory stimulation, with a decrease in correlation between neighbouring pixels. The diffuse activation in response to forelimb stimulation observed in those previous works is in agreement with our results that reveal the absence of a clear pattern of cortical propagation, as highlighted by low smoothness, in the acute phase after stroke.

These differences decline during weeks of motor training in the robot group, in fact by the second week of training duration reaches values comparable to healthy mice. We also show that the smoothness was on average comparable to healthy mice after robotic training. Our findings on the chronic phase of the robot group are in agreement with what we observed in (***Conti et al., 2020***) where repetitive motor training induced a task-dependent spatial segregation similar to healthy mice though unaccompanied by functional recovery (***Spalletti et al., 2017***).

Comparison of different rehabilitation paradigms

Combined rehabilitation profoundly altered the propagation of global events as compared to both healthy (control) and motor trained stroke (robot) mice. While during the chronic phase of robot mice no significant differences were observed in cortical directionality propagation with respect to healthy animals, the combined rehabilitative treatment presented a different profile compared to the other groups. More in detail, rehab mice show a decrease of duration and greater smoothness with respect to control and robot mice indicating the arrangement of a fast and directed pattern of propagation. Temporally compressed and reliable cortical activity sequences may be associated with a more effective trigger of subcortical movement machinery (***Makino et al., 2017***).

In addition, the substantial increase in smoothness after combined rehabilitation finds a nice correlate in the segregation of motor representation illustrated in preclinical (***Allegra Mascaro et al., 2019***) and clinical studies (***Chang et al., 2012***). In these works, improved motor functionality induced by post-stroke combined rehabilitation is associated with a more focused brain activation during the execution of a motor task. (***Conti et al., 2020***). Importantly, generalised recovery in

bioRxiv preprint doi: https://doi.org/10.1101/2020.07.10.197509; this version posted July 11, 2020. The copyright holder for this preprint (which was not certified by peer review) is the author/funder, who has granted bioRxiv a license to display the preprint in perpetuity. It is made available under a CC-BY-NC-ND 4.0 International license.
Manuscript submitted to eLife

rehab mice, see (***Spalletti et al., 2017***; ***Allegra Mascaro et al., 2019***) is not necessarily associated with recovery of pre-stroke spatiotemporal propagation features. Indeed, the results on all motor-evoked spatiotemporal propagation indicators suggest that the combination of contralesional inactivation and motor training acts towards the establishment of a new propagation pattern rather than the restoration of pre-stroke features.

In summary, our detailed spatiotemporal analysis of global activation patterns during longitudinal motor training provides a powerful non-invasive tool to quantify the relative success of different state-of-the-art rehabilitation paradigms. The propagation-based biomarkers deliver new and unforeseen information about the brain mechanisms underlying motor recovery and this could pave the way towards a more targeted post-stroke therapy. As a final remark, we would like to stress that the method used here is universal and could easily be adapted to functional techniques (including electroencephalography and functional Magnetic Resonance Imaging) in many other clinical settings. For example, it could be extended to disorders of the central nervous system similarly associated with alterations in the spatiotemporal propagation of brain activity, from traumatic brain injury to autism.

Materials and methods

Experimental design

Mice

All experimental procedures were performed in accordance with directive 2010/63/EU on the protection of animals used for scientific purposes and approved by the Italian Minister of Health, authorization n.183/2016-PR. Mice were housed in clear plastic cages under a 12 h light/dark cycle and were given ad libitum access to water and food. We used a transgenic mouse line (C57BL/6J-Tg(Thy1GCaMP6f)GP5.17Dkim/J, referred to as GCaMP6f mice) expressing a genetically-encoded fluorescent calcium indicator under the control of the Thy-1 promoter. Mice were identified by earmarks and numbered accordingly. Animals were randomly assigned to 3 experimental groups (control, robot and rehab). Each group contained comparable numbers of male and female mice (weighing approximately 25g). The age of mice (ranging from 6 to 8 months old) was consistent between the groups.

Photothrombotic Stroke Induction & Optical Window

All surgical procedures were performed under Isoflurane anesthesia (3% induction, 1.5% maintenence, in 1.5L/min oxygen). The animals (apart from the control mice) were placed into a stereotaxic apparatus (Stoelting, Wheat Lane, Wood Dale, IL 60191) and, after removing the skin over the skull and the periosteum, the primary motor cortex (M1) was identified (stereotaxic coordinates 1,75 lateral, 0.5 anterior to bregma). Five minutes after intraperitoneal injection of Rose Bengal (0.2 ml, 10 mg/ml solution in Phosphate Buffer Saline (PBS); Sigma Aldrich, St. Louis, Missouri, USA), white light from an LED lamp (CL 6000 LED, Carl Zeiss Microscopy, Oberkochen, Germany) was focused with a 20X objective (EC Plan Neofluar NA 0.5, Carl Zeiss Microscopy, Oberkochen, Germany) and used to illuminate the M1 for 15 min to induce unilateral stroke in the right hemisphere. Botulinum Neurotoxin E (BoNT/E) injections in rehab mice were performed during the same surgical session of the photothrombotic lesions. We used a dental drill to create a small craniotomy over M1 of the healthy hemisphere. Then 500 nL of BoNT/E were delivered in two separate injections. A cover glass and an aluminum headpost were attached to the skull using transparent dental cement (Super Bond, C&S). Afterwards, the animals were placed in their cages until full recovery.

Motor Training Protocol on the M-Platform

Before the first imaging session each mouse was allowed to become accustomed to the apparatus. The animals were trained by means of the M-Platform, which is a robotic system that encourages mice to perform a retraction movement of their left forelimb (***Spalletti et al., 2014***; ***Allegra Mascaro***

bioRxiv preprint doi: https://doi.org/10.1101/2020.07.10.197509; this version posted July 11, 2020. The copyright holder for this preprint (which was not certified by peer review) is the author/funder, who has granted bioRxiv a license to display the preprint in perpetuity. It is made available under a CC-BY-NC-ND 4.0 International license.

et al., 2019). The training consisted of up to 15 cycles of passive extension of the affected forelimb followed by its active retraction triggered by an acoustic cue. All groups performed at least four weeks (20 sessions) of daily training; in addition, 5 out of 8 robot mice were also recorded for one week before stroke (5 sessions).

Wide-Field Fluorescence Microscopy

The custom-made wide-field imaging setup (*Crocini et al., 2016*; *Conti et al., 2019*) was equipped with a 505 nm LED (M505L3 Thorlabs, New Jersey, United States) light was deflected by a dichroic filter (DC FF 495-DI02 Semrock, Rochester, New York USA) on the objective (2.5x EC Plan Neofluar, NA 0.085, Carl Zeiss Microscopy, Oberkochen, Germany). Then a 20x objective (LD Plan Neofluar, 20x/0.4 M27, Carl Zeiss Microscopy, Oberkochen, Germany) was used to demagnify the image onto a high-speed complementary metal-oxide semiconductor (CMOS) sensor (OrcaFLASH 4.0, Hamamatsu Photonics, NJ, USA). The fluorescence signal was selected by a band pass filter (525/50 Semrock, Rochester, New York USA) and images (100 x 100 pixels, pixel size 60 μm) were acquired at 25 Hz.

Signal processing and data analysis

Preprocessing

Data acquired during each recording session (one mouse, one day, see Figure 1b) was processed offline using custom routines implemented in Python (Python Software Foundation) and Matlab (MathWorks). Each such dataset consisted of up to 15 cycles of active retraction movements on a slide triggered by passively actuated contralesional forelimb extensions. To ensure the consistency of the field of view across sessions and across mice, each frame of the fluorescence data was offline registered by aligning each frame to two reference points (corresponding to bregma and lambda) that were previously marked on the glass window during the surgery procedure. For the 2D fluorescence data, masking the region of interest and spatial downsampling by a factor 3 for both rows and columns resulted in calcium activity matrices of 12 x 21 (or sometimes 12 x 19) pixels. Spatial average over all pixels yielded the mean calcium activity. In parallel, the force applied to the slide by the mouse and the discrete status of the slide were recorded. Using samplings with a time step of 40 ms and acquisition times of up to 400 seconds this yielded recordings with at most 10000 data points. The calcium traces were detrended via subtraction of a moving average of order 75 (three seconds) and, in order to yield a better time resolution, upsampled by a factor 20.

Event detection

Next, within all of these traces we identified the times of the most relevant discrete events. For the status (Figure 2a) we marked the transition from level 3 to level 4 which corresponds to the completion of the forelimb retraction by the active movement of the mouse upon which the animal received its reward (reward pulling event). For the force (Figure 2b), the mean calcium (Figure 2c) and the individual calcium traces of all the pixels the events are the high-amplitude peaks that can easily be recognised. As event times we used the upwards crossings of a threshold T which in each of these cases was defined in a data-adaptive manner according to $T = mean(x) + t * std(x)$. The free parameter t was set to 1.5 for the force and 1.7 for all the calcium traces. In the slower calcium traces, in order to avoid double detections due to noise, we discarded all events that succeeded the previous event by less than a minimum inter-event interval of 25 data points (one second).

SPIKE-order

The events (from now on called spikes) of all the pixels can be represented best in a rasterplot like the one shown in Figure 2d. The next important step was to identify the global events that correspond to the events of the mean calcium trace. To this aim, we used the cSPIKE-implementation (*Satuvuori et al., 2017*) of the SPIKE-order approach recently proposed in *Kreuz et al.* (*2017*) (for

bioRxiv preprint doi: https://doi.org/10.1101/2020.07.10.197509; this version posted July 11, 2020. The copyright holder for this preprint (which was not certified by peer review) is the author/funder, who has granted bioRxiv a license to display the preprint in perpetuity. It is made available under a CC-BY-NC-ND 4.0 International license.
Manuscript submitted to eLife

detailed definitions of all the underlying quantities please refer to the Appendix). The original proposal was designed for rather clean data with well-defined global events. These conditions hold for most of our datasets as well, however, we added a few tailor-made denoising steps that addressed the rare instances of increased noisiness that we observed in some of the datasets.

The procedure consisted of six steps: in an initial denoising step, we filtered out all spikes of individual pixels that were not within 1 second of a mean calcium event and thus were certainly not part of global events. Secondly, we applied the coincidence detection first introduced for the bivariate measure *event synchronization* (***Quian Quiroga et al., 2002***). This criterion paired spikes in such a way that every spike was matched with at most one spike in each of the other pixels. Here we combined the original adaptive approach with a maximum allowed distance between spikes of 2.5 seconds. Next, we used the symmetric and multivariate measure SPIKE-Synchronization C (***Kreuz et al., 2015***) to quantify for each spike the fraction of other pixels for whom a matching spike could be found. By setting a threshold value $C_{thr} = 0.75$ we only took into account spikes which were coincident with spikes in at least three quarters of the other pixels, all other spikes were filtered out as background noise.

In a fourth step, we applied the SPIKE-order D (***Kreuz et al., 2017***) which evaluates the temporal order of the spikes by quantifying for each spike the net-fraction of spikes of other pixels this spike is leading (positive value) or following (negative value). Based on the time profile we identified start and end spikes of global events by tracking the jumps from a negative local minimum (last spike of previous event) to a positive local maximum (first spike of current event). In one further denoising step we discarded split events and eliminated outlier spikes by using a maximum distance between consecutive spikes of 0.15 seconds and thereby kept only continuous global events. The final step used in the visualisation of the spike trains in Figure 2d involved the Synfire Indicator (***Kreuz et al., 2017***), a scalar measure which quantifies to what degree the spatiotemporal propagation patterns of the global events are consistent with each other. Optimisation of this indicator was used to sort the spike trains / pixels from overall leader to overall follower. Here, overall means that we take into account all global events at the same time. The result is that the first spike trains contain mostly leading spikes, whereas the last spike trains consist largely of trailing spikes.

Categorisation of events

Next, we divided the global events into several types using the following three-level categorisation scheme (the corresponding branching structure is shown in Section Methods): First, we separated all the global events that are not associated with a force event (non-Force, **nF**). For this we demanded that there is no force event in the interval [1 second before, 0.75 seconds after] the matching calcium event. The window was slightly asymmetric to account for the fact that typically Force were observed a bit earlier than mean calcium events. The remaining Force events (**F**) were further subdivided into events that occur during the passive extension of the arm by the slide (Passive, **Pass**) and events that occur outside that window (Active, **Act**). In the passive events the mouse applied force to resist the forelimb extension movement of the robot, whereas the active events were the ones where the force was applied during an active retraction movement (when the status variable was set to 3, i.e. between the Go cue and the completion of the task). Finally, among the active events we distinguished between events which were not completed and thus not rewarded (non-Reward Pulling, **nRP**) and events which lead to a completion of the forelimb retraction and therefore were rewarded (Reward Pulling, **RP**). The categorisation criterion was the occurrence of a transition from status 3 to status 4 within [0.75 seconds before, 0.75 seconds after] a calcium event. This window was symmetric, since the observed temporal distribution of status events was symmetric with respect to the mean calcium events.

Three propagation indicators: Duration, Angle, Smoothness

For all global events, the event time was defined as the average time of all the spikes within the event and our first propagation indicator, the event duration, was defined as time from the first to

bioRxiv preprint doi: https://doi.org/10.1101/2020.07.10.197509; this version posted July 11, 2020. The copyright holder for this preprint (which was not certified by peer review) is the author/funder, who has granted bioRxiv a license to display the preprint in perpetuity. It is made available under a CC-BY-NC-ND 4.0 International license.

the last spike of the event. To calculate the other two propagation indicators, angle and smoothness, we first generated the propagation matrix by mapping the color-coded relative order of the spikes onto the pixels of the 2D-recording plane (compare Figure 2f). Next, we applied singular value decomposition (SVD, ***Yanai et al.*** (***2011***)) which searches for spatial patterns by decomposing the propagation matrix P into three simple transformations: a rotation U, a scaling Σ along the rotated coordinate axes and a second rotation V^T.

The rotations U and V^T are orthonormal matrices and Σ is a diagonal matrix containing in its diagonal the singular values σ_i of P. By backprojecting the sorted singular values one at a time

$$\Sigma_1 = \begin{bmatrix} \sigma_1 & & & \\ & 0 & & \\ & & 0 & \\ & & & \ddots \end{bmatrix} \qquad \Sigma_2 = \begin{bmatrix} 0 & & & \\ & \sigma_2 & & \\ & & 0 & \\ & & & \ddots \end{bmatrix}$$

we could obtain various projections of the original propagation matrix

$$P_1 = U\Sigma_1 V^T \qquad P_2 = U\Sigma_2 V^T$$

. The mean gradients with respect to column (c) and row (r) increments of the first two projections were calculated as

$$\begin{cases} g_1^c = \mathbb{E}(-\frac{\partial P_1}{\partial c}) \\ g_1^r = \mathbb{E}(-\frac{\partial P_1}{\partial r}) \end{cases} \qquad \begin{cases} g_2^c = \mathbb{E}(-\frac{\partial P_2}{\partial c}) \\ g_2^r = \mathbb{E}(-\frac{\partial P_2}{\partial r}) \end{cases}$$

with $\mathbb{E}$ denoting the average across pixels while the sign (-) is defined by the directionality in the matrix P going from leader (+1) to follower (-1). The main propagation directions, along the column and row directions,

$$\begin{cases} v^c = \sigma_1 g_1^c + \sigma_2 g_2^c \\ v^r = \sigma_1 g_1^r + \sigma_2 g_2^r \end{cases}$$

were calculated from the weighted average of the mean gradients of the first two projections, with the singular values as weights. Our second propagation indicator, the angle

$$\alpha = \arctan\left(\frac{v^c}{v^r}\right)$$

was defined relative to the horizontal axis.

Finally, our third propagation indicator, the smoothness S, quantified how well the second order approximation, the weighted sum of the projections of only the first two singular values, captures the full spatiotemporal pattern obtained by considering all singular values σ_i. Smoothness is defined as the relative weight of the first two approximations

$$S = \frac{\sigma_1^2 + \sigma_2^2}{\sum_i \sigma_i^2}. \tag{1}$$

Statistical Tests

Statistical tests were carried out separately for all three propagation indicators (angle, smoothness, duration) and for each condition: control group (Fig. 4), acute phase (Fig. 5) and rehabilitation comparisons (Fig. 6). Control group models analyse the behaviours of healthy mice only during all four weeks of motor training. Acute phase models use the first week post-stroke of robot mice, the first week of control mice and the pre-stroke week of robot mice, considered here as control ones. Finally, the rehabilitation comparisons look at the weeks from the second to the fourth of all control, robot and rehab mice.

For smoothness and duration, differences in means were tested using estimates of mixed effect models implemented in *R* (package *lme4*, ***Bates et al., 2015***). All models started with a full parametrisation of both fixed and random effects, backward selection through ANOVA and RANOVA, respectively, selected a parsimonious feasible model without removing relevant effects that

bioRxiv preprint doi: https://doi.org/10.1101/2020.07.10.197509; this version posted July 11, 2020. The copyright holder for this preprint (which was not certified by peer review) is the author/funder, who has granted bioRxiv a license to display the preprint in perpetuity. It is made available under a CC-BY-NC-ND 4.0 International license.

could decrease the Type I error rate and increase the statistical power (***Matuschek et al., 2017***). Differences in least squares means and their p-value were estimated with the *R* package *lmerTest* (***Kuznetsova et al., 2017***). The Holm-Bonferroni correction for multiple comparisons was used to obtain the statistical significance scores. Normality of residuals assumption was tested with the Kolmogorov-Smirnov test, while homogeneity of variance for fixed effects without related random slope was evaluated with the Breusch-Pagan test. If normality assumption did not hold, a Box-Cox transform of the dependent variable (***Gurka et al., 2006***) was carried out. If the Breusch-Pagan test revealed departure from homogeneity of variance, we look at which comparisons had different variances and results were again corrected with the Holm-Bonferroni method for multiple comparisons.

For the propagation angle we focused on the differences in circular variance, tested with multiple Bartlett tests (*R* package *circular*, ***Agostinelli and Lund, 2017***). Then, once more the Holm-Bonferroni correction was adopted to correct the multiple comparison bias. Assumption of Von-Mises distribution for both groups under comparison was tested with the Watson test (***Jammalamadaka and Sengupta, 2001***).

Acknowledgments

We thank Cristina Spalletti for a very careful reading of the manuscript. This project has received funding from the H2020 EXCELLENT SCIENCE - European Research Council (ERC) under grant agreement ID n. 692943 BrainBIT and from the European Union's Horizon 2020 Research and Innovation Programme under Grant Agreement No. 785907 (HBP SGA2) and and No. 945539 (HBP SGA3). The authors declare that they have no known competing financial interests or personal relationships that could have appeared to influence the work reported in this paper.

bioRxiv preprint doi: https://doi.org/10.1101/2020.07.10.197509; this version posted July 11, 2020. The copyright holder for this preprint (which was not certified by peer review) is the author/funder, who has granted bioRxiv a license to display the preprint in perpetuity. It is made available under a CC-BY-NC-ND 4.0 International license.

Appendix

Here we present the more detailed definitions of the SPIKE-order approach, the central method of our study that we use to identify global events and to track the propagation patterns within these events by sorting the spikes from leader to follower.

Adaptive Coincidence Detection

Analysing leader-follower relationships in a spike train set requires a criterion that determines which spikes should be compared against each other. Here we use the adaptive coincidence criterion first proposed in ***Quian Quiroga et al.*** (***2002***). This coincidence detection is scale- and parameter-free since the maximum time lag $\tau_{ij}^{(m,n)}$ up to which two spikes $t_i^{(m)}$ and $t_j^{(n)}$ of spike trains $m, n = 1, ..., N$ (with N denoting the number of spike trains) are considered to be synchronous is adapted to the local firing rates according to

$$\begin{aligned}\tau_{ij}^{(m,n)} = \min\{&t_{i+1}^{(m)} - t_i^{(m)}, t_i^{(m)} - t_{i-1}^{(m)},\\ &t_{j+1}^{(n)} - t_j^{(n)}, t_j^{(n)} - t_{j-1}^{(n)}\}/2.\end{aligned} \tag{2}$$

SPIKE-Synchronization

Following ***Kreuz et al.*** (***2015***), we apply the adaptive coincidence criterion in a multivariate context by defining for each spike i of any spike train n and for each other spike train m a coincidence indicator

$$C_i^{(n,m)} = \begin{cases} 1 & \text{if } \min_j(|t_i^{(n)} - t_j^{(m)}|) < \tau_{ij}^{(n,m)} \\ 0 & \text{otherwise.} \end{cases} \tag{3}$$

which is either one or zero depending on whether this spike is part of a coincidence with a spike of spike train m or not. This results in an unambiguous spike matching since any spike can at most be coincident with one spike (the nearest one) in the other spike train.

Subsequently, for each spike of every spike train a normalised coincidence counter

$$C_i^{(n)} = \frac{1}{N-1} \sum_{m \neq n} C_i^{(n,m)} \tag{4}$$

is obtained by averaging over all $N - 1$ bivariate coincidence indicators involving the spike train n.

In order to obtain a single multivariate SPIKE-Synchronization profile we pool the coincidence counters of all the spikes of every spike train:

$$\{C(t_k)\} = \bigcup_n \{C_{i(k)}^{(n(k))}\}, \tag{5}$$

where we map the spike train indices n and the spike indices i into a global spike index k denoted by the mapping $i(k)$ and $n(k)$.

With M denoting the total number of spikes in the pooled spike train, the average of this profile

$$S_C = \begin{cases} \frac{1}{M} \sum_{k=1}^{M} C(t_k) & \text{if } M > 0 \\ 1 & \text{otherwise} \end{cases} \tag{6}$$

yields SPIKE-Synchronization, the overall fraction of coincidences. It reaches one if and only if each spike in every spike train has one matching spike in all the other spike trains (or if there are no spikes at all), and it attains the value zero if and only if the spike trains do not contain any coincidences.

SPIKE-Order

While SPIKE-Synchronization is invariant to which of the two spikes within a coincidence is leading and which is following, the temporal order of the spikes is taken into account by the two indicators SPIKE-Order and Spike Train Order.

bioRxiv preprint doi: https://doi.org/10.1101/2020.07.10.197509; this version posted July 11, 2020. The copyright holder for this preprint (which was not certified by peer review) is the author/funder, who has granted bioRxiv a license to display the preprint in perpetuity. It is made available under a CC-BY-NC-ND 4.0 International license.
Manuscript submitted to Chaos

The bivariate anti-symmetric SPIKE-Order indicators

$$\begin{aligned} D_i^{(n,m)} &= C_i^{(n,m)} \cdot \mathrm{sign}(t_{j'}^{(m)} - t_i^{(n)}) \\ D_{j'}^{(m,n)} &= C_{j'}^{(m,n)} \cdot \mathrm{sign}(t_i^{(n)} - t_{j'}^{(m)}) = -D_i^{(n,m)}, \end{aligned} \tag{7}$$

where the index j' is defined from the minimum in Eq. 3 as $j' = \arg\min_j(|t_i^{(1)} - t_j^{(2)}|)$, assign to each spike either a 1 or a -1 depending on whether the respective spike is leading or following a coincident spike in the other spike train.

SPIKE-Order distinguishes leading and following spikes, and is thus used for color-coding the individual spikes on the leader to follower scale. But it can also be employed to sort the *spike trains* based on a pairwise analysis. For this we use the cumulative SPIKE-Order matrix

$$D^{(n,m)} = \sum_i D_i^{(n,m)}. \tag{8}$$

This anti-symmetric matrix sums up the orders of coincidences from the respective pair of spike trains only and quantifies how much spike train n is leading spike train m. Hence if $D^{(n,m)} > 0$ spike train n is leading m, while $D^{(n,m)} < 0$ means m is leading n. If the current spike train order is consistent with the synfire property (i.e., it displays consistent repetitions of the same global propagation pattern), we thus expect that $D^{(n,m)} > 0$ for $n < m$ and $D^{(n,m)} < 0$ for $n > m$. Therefore, we construct the overall SPIKE-Order as

$$D_< = \sum_{n<m} D^{(n,m)}, \tag{9}$$

i.e. the sum over the upper right tridiagonal part of the matrix $D^{(n,m)}$.

Synfire Indicator

After normalizing by the overall number of possible coincidences, we arrive at the definition of the Synfire Indicator:

$$F = \frac{2D_<}{(N-1)M}. \tag{10}$$

This measure quantifies to what degree coinciding spike pairs with correct order prevail over coinciding spike pairs with incorrect order, or in other words, to what extent the spike trains in their current order resemble a synfire pattern. Conversely, the maximization of the Synfire Indicator as a function of the spike train order within a set of spike trains can be used to sort spike trains from leader to follower such that the set comes as close as possible to a synfire pattern. Denoting the Synfire Indicator for any given spike train index permutation $\varphi(n)$ as F_φ, the optimal (**s**orted) order φ_s is the one resulting in the maximal overall Synfire Indicator $F_s = F_{\varphi_s}$:

$$\varphi_s : F_{\varphi_s} = \max_\varphi\{F_\varphi\} = F_s. \tag{11}$$

Whereas the Synfire Indicator F_φ for any spike train order φ is normalized between -1 and 1, the optimized Synfire Indicator F_s can only attain values between 0 and 1. A perfect synfire pattern results in $F_s = 1$, while sufficiently long Poisson spike trains without any synfire structure yield $F_s \approx 0$. For details on the optimisation procedure, please refer to ***Kreuz et al.*** (***2017***).

Source Codes

SPIKE-Synchronization, SPIKE-Order and Spike Train Order are implemented in three publicly available software packages. Results in this study were obtained using cSPIKE [1] (Matlab command line with MEX-files). The Matlab-based graphical user interface SPIKY [2] (***Kreuz et al., 2015***), or the Python

[1] http://www.fi.isc.cnr.it/users/thomas.kreuz/Source-Code/cSPIKE.html
[2] http://www.fi.isc.cnr.it/users/thomas.kreuz/Source-Code/SPIKY.html

bioRxiv preprint doi: https://doi.org/10.1101/2020.07.10.197509; this version posted July 11, 2020. The copyright holder for this preprint (which was not certified by peer review) is the author/funder, who has granted bioRxiv a license to display the preprint in perpetuity. It is made available under a CC-BY-NC-ND 4.0 International license.
Manuscript submitted to eLife

library PySpike [3] (***Mulansky and Kreuz, 2016***) are available as well.

Caption Supplementary Movie 1

Movie depicting the propagation of activity during the training cycle shown in Figure 1c. As the vertical green line superimposed over subplots (a) to (d) moves forward in time (from -0.12 seconds before to 1.28 seconds after the threshold crossing of the force), in the Calcium image in subplot (e) a propagation of activity from left to right can be seen. This is in accordance with the propagation matrix shown in subplot (f) which color-codes the temporal order of activation from leader (red) to follower (blue). (a) Status of the robotic sled. (b) Force applied by the mouse during the retraction movement. (c) Average calcium signal over all pixels. (d) Raster plot obtained from the threshold crossings of individual pixels versus time. (e) Calcium imaging sequence of cortical activation, superimposed on the standard atlas of brain regions. (f) The propagation matrix is obtained by projecting the relative order of these threshold crossings onto the 2D-recording plane.

Panel	Indicator	Event type	Value
a	Number of events	F	492
		nF	45
		Act	356
		Pass	136
		RP	277
		nRP	79
b	Smoothness		0.41
	Angle		-3.11
c	Smoothness		0.78
	Angle		-1.46
d	Smoothness		0.87
	Angle		0.09
e	Smoothness	F	0.67 ± 0.05
		nF	0.56 ± 0.06
	Angle	F	0.40 ± 0.49
		nF	0.63 ± 0.81
f	Smoothness	Act	0.67 ± 0.06
		Pass	0.67 ± 0.05
	Angle	Act	0.45 ± 0.44
		Pass	0.27 ± 0.58
g	Smoothness	RP	0.68 ± 0.05
		nRP	0.65 ± 0.06
	Angle	RP	0.46 ± 0.43
		nRP	0.44 ± 0.52

Appendix 0 Table 1. Values for Figure 3

Panel	Indicator	Event type	Group	Diff. type	p-value	
c	Angle	F-nF	Control	Variance	10^{-10}	⋆⋆⋆
		Act-Pass			10^{-9}	⋆⋆⋆
		RP-nRP			10^{-8}	⋆⋆⋆
e	Smoothness	F-nF			0.001	⋆⋆
		RP-nRP			0.001	⋆⋆
g	Duration	Act-Pass			0.002	⋆⋆

Appendix 0 Table 2. Values for Figure 4

[3] http://www.pyspike.de

bioRxiv preprint doi: https://doi.org/10.1101/2020.07.10.197509; this version posted July 11, 2020. The copyright holder for this preprint (which was not certified by peer review) is the author/funder, who has granted bioRxiv a license to display the preprint in perpetuity. It is made available under a CC-BY-NC-ND 4.0 International license.
Manuscript submitted to eLife

Panel	Indicator	Event type	Group	Diff. type	p-value	
b	Angle	F - nF	Control	Variance	10^{-7}	⋆ ⋆ ⋆
			Stroke		10^{-5}	⋆ ⋆ ⋆
		Act - Pass	Control		10^{-4}	⋆ ⋆ ⋆
			Stroke		0.046	⋆
c	Smoothness		Control - Stroke	Mean	0.007	**
d		F - nF	Control		10^{-10}	***
		F	Control - Stroke		0.004	**
		Act	Control - Stroke		0.01	*
		Pass	Control - Stroke		0.002	**
		RP-nRP	Control		0.008	**
		RP	Control - Stroke		0.005	**
e	Duration		Control - Stroke		0.003	**
f		F	Control - Stroke		0.026	*
		Act-Pass	Control		0.042	*
		Act	Control - Stroke		0.034	*
		Pass	Control - Stroke		0.035	*
		RP	Control - Stroke		0.014	*
		nRP	Control - Stroke		0.028	*

Appendix 0 Table 3. Values for Figure 5

References

Afrashteh N, Inayat S, Mohsenvand M, Mohajerani MH. Optical-flow analysis toolbox for characterization of spatiotemporal dynamics in mesoscale optical imaging of brain activity. Neuroimage. 2017; 153:58–74.

Agostinelli C, Lund U. R package `circular`: Circular Statistics (version 0.4-93). CA: Department of Environmental Sciences, Informatics and Statistics, Ca' Foscari University, Venice, Italy. UL: Department of Statistics, California Polytechnic State University, San Luis Obispo, California, USA; 2017, https://r-forge.r-project.org/projects/circular/.

Allegra Mascaro AL, Conti E, Lai S, Di Giovanna AP, Spalletti C, Alia C, Panarese A, Scaglione A, Sacconi L, Micera S, Caleo M, Pavone FS. Combined Rehabilitation Promotes the Recovery of Structural and Functional Features of Healthy Neuronal Networks after Stroke. Cell Rep. 2019 Sep; 28(13):3474–3485.e6.

Allen WE, Kauvar IV, Chen MZ, Richman EB, Yang SJ, Chan K, Gradinaru V, Deverman BE, Luo L, Deisseroth K. Global Representations of Goal-Directed Behavior in Distinct Cell Types of Mouse Neocortex. Neuron. 2017 May; 94(4):891–907.e6.

Balbi M, Vanni MP, Vega MJ, Silasi G, Sekino Y, Boyd JD, LeDue JM, Murphy TH. Longitudinal monitoring of mesoscopic cortical activity in a mouse model of microinfarcts reveals dissociations with behavioral and motor function. J Cereb Blood Flow Metab. 2018 Mar; p. 0271678X18763428.

Bates D, Mächler M, Bolker B, Walker S. Fitting Linear Mixed-Effects Models Using lme4. Journal of Statistical Software. 2015; 67(1):1–48. doi: 10.18637/jss.v067.i01.

Brier LM, Landsness EC, Snyder AZ, Wright PW, Baxter GA, Bauer AQ, Lee JM, Culver JP. Separability of calcium slow waves and functional connectivity during wake, sleep, and anesthesia. Neurophotonics. 2019; 6(3):035002.

Brown CE, Aminoltejari K, Erb H, Winship IR, Murphy TH. In vivo voltage-sensitive dye imaging in adult mice reveals that somatosensory maps lost to stroke are replaced over weeks by new structural and functional circuits with prolonged modes of activation within both the peri-infarct zone and distant sites. Journal of Neuroscience. 2009; 29(6):1719–1734.

Burke Quinlan E, Dodakian L, See J, McKenzie A, Le V, Wojnowicz M, Shahbaba B, Cramer SC. Neural function, injury, and stroke subtype predict treatment gains after stroke. Annals of neurology. 2015; 77(1):132–145.

Carandini M, Shimaoka D, Rossi LF, Sato TK, Benucci A, Knöpfel T. Imaging the awake visual cortex with a genetically encoded voltage indicator. J Neurosci. 2015 Jan; 35(1):53–63.

Carter AR, Astafiev SV, Lang CE, Connor LT, Rengachary J, Strube MJ, Pope DLW, Shulman GL, Corbetta M. Resting interhemispheric functional magnetic resonance imaging connectivity predicts performance after stroke. Ann Neurol. 2010 Mar; 67(3):365–375.

bioRxiv preprint doi: https://doi.org/10.1101/2020.07.10.197509; this version posted July 11, 2020. The copyright holder for this preprint (which was not certified by peer review) is the author/funder, who has granted bioRxiv a license to display the preprint in perpetuity. It is made available under a CC-BY-NC-ND 4.0 International license.

Panel	Indicator	Event type	Group	Diff. type	p-value	
b	Angle	F	Control - Rehab	Variance	10^{-8}	⋆⋆⋆
			Robot - Rehab		10^{-8}	⋆⋆⋆
		Act	Control - Rehab		10^{-9}	⋆⋆⋆
			Robot - Rehab		10^{-9}	⋆⋆⋆
		Pass	Control - Rehab		0.027	⋆
			Robot - Rehab		0.008	⋆⋆
		RP	Control - Rehab		10^{-9}	⋆⋆⋆
			Robot - Rehab		10^{-9}	⋆⋆⋆
		nRP	Control - Robot		0.024	⋆
			Robot - Rehab		10^{-5}	⋆⋆⋆
c	Smoothness		Control - Rehab	Mean	0.025	*
			Robot - Rehab		10^{-4}	***
d		F	Robot - Rehab		0.001	**
		nF	Control - Rehab		0.018	*
			Robot - Rehab		0.002	**
		Act	Control - Robot		0.046	*
			Robot - Rehab		10^{-6}	***
		Pass	Control - Rehab		0.030	*
			Robot - Rehab		10^{-6}	***
		RP	Control - Rehab		0.029	*
			Robot - Rehab		10^{-5}	***
		nRP	Control - Rehab		0.014	*
			Robot - Rehab		10^{-4}	***
e	Duration		Control - Rehab		10^{-4}	***
			Robot - Rehab		10^{-6}	***
f		F	Control - Rehab		0.002	**
			Robot - Rehab		10^{-5}	***
		nF	Control - Rehab		0.002	**
			Robot - Rehab		10^{-5}	***
		Act	Control - Rehab		0.002	**
			Robot - Rehab		10^{-4}	***
		Pass	Control - Rehab		10^{-4}	***
			Robot - Rehab		10^{-5}	***
		RP	Control - Rehab		0.003	**
			Robot - Rehab		10^{-6}	***
		nRP	Control - Rehab		0.002	**
			Robot - Rehab		10^{-6}	***

Appendix 0 Table 4. Values for Figure 6

Carter AR, Patel KR, Astafiev SV, Snyder AZ, Rengachary J, Strube MJ, Pope A, Shimony JS, Lang CE, Shulman GL, Corbetta M. Upstream dysfunction of somatomotor functional connectivity after corticospinal damage in stroke. Neurorehabil Neural Repair. 2012 Jan; 26(1):7–19.

Cassidy JM, Wodeyar A, Wu J, Kaur K, Masuda AK, Srinivasan R, Cramer SC. Low-Frequency Oscillations Are a Biomarker of Injury and Recovery After Stroke. Stroke. 2020 Apr; p. STROKEAHA120028932.

Celotto M, De Luca C, Resta PMF, Allegra Mascaro AL, Pavone FS, De Bonis G, Paolucci PS. Analysis and Model of Cortical Slow Waves Acquired with Optical Techniques. Methods and Protocols. 2020; 3(1):14.

Chang WH, Kim YH, Yoo WK, Goo KH, Park Ch, Kim ST, Pascual-Leone A. rTMS with motor training modulates cortico-basal ganglia-thalamocortical circuits in stroke patients. Restorative neurology and neuroscience. 2012; 30(3):179–189.

Chen CC, Lee SH, Wang WJ, Lin YC, Su MC. EEG-based motor network biomarkers for identifying target patients with stroke for upper limb rehabilitation and its construct validity. PLOS ONE. 2017 06; 12(6):1–20. https://doi.org/10.1371/journal.pone.0178822, doi: 10.1371/journal.pone.0178822.

Chen TW, Wardill TJ, Sun Y, Pulver SR, Renninger SL, Baohan A, Schreiter ER, Kerr RA, Orger MB, Jayaraman V, Looger LL, Svoboda K, Kim DS. Ultrasensitive fluorescent proteins for imaging neuronal activity. Nature. 2013 Jul; 499(7458):295–300.

bioRxiv preprint doi: https://doi.org/10.1101/2020.07.10.197509; this version posted July 11, 2020. The copyright holder for this preprint (which was not certified by peer review) is the author/funder, who has granted bioRxiv a license to display the preprint in perpetuity. It is made available under a CC-BY-NC-ND 4.0 International license.

Clancy KB, Orsolic I, Mrsic-Flogel TD. Locomotion-dependent remapping of distributed cortical networks. Nat Neurosci. 2019 May; 22(5):778–786.

Conti E, Allegra Mascaro AL, Scaglione A, de Vito G, Calugi F, Pasquini M, Pizzorusso T, Micera S, Pavone FS. Synergic effect of optogenetic stimulation and motor training boosts recovery of motor functionality after stroke supported by segregation of motor representation. bioRxiv. 2020; https://www.biorxiv.org/content/early/2020/03/06/2020.03.05.974972, doi: 10.1101/2020.03.05.974972.

Conti E, Mascaro A, Letizia A, Pavone FS. Large Scale Double-Path Illumination System with Split Field of View for the All-Optical Study of Inter-and Intra-Hemispheric Functional Connectivity on Mice. Methods and protocols. 2019; 2(1):11.

Crocini C, Ferrantini C, Coppini R, Scardigli M, Yan P, Loew LM, Smith G, Cerbai E, Poggesi C, Pavone FS, et al. Optogenetics design of mechanistically-based stimulation patterns for cardiac defibrillation. Scientific reports. 2016; 6:35628.

Dijkhuizen RM, Singhal AB, Mandeville JB, Wu O, Halpern EF, Finklestein SP, Rosen BR, Lo EH. Correlation between brain reorganization, ischemic damage, and neurologic status after transient focal cerebral ischemia in rats: a functional magnetic resonance imaging study. Journal of Neuroscience. 2003; 23(2):510–517.

Greenberg A, Abadchi JK, Dickson CT, Mohajerani MH. New waves: Rhythmic electrical field stimulation systematically alters spontaneous slow dynamics across mouse neocortex. Neuroimage. 2018 Jul; 174:328–339.

Gurka MJ, Edwards LJ, Muller KE, Kupper LL. Extending the Box–Cox transformation to the linear mixed model. Journal of the Royal Statistical Society: Series A (Statistics in Society). 2006; 169(2):273–288.

Harrison TC, Silasi G, Boyd JD, Murphy TH. Displacement of sensory maps and disorganization of motor cortex after targeted stroke in mice. Stroke. 2013; 44(8):2300–2306.

Haupt D, Vanni MP, Bolanos F, Mitelut C, LeDue JM, Murphy TH. Mesoscale brain explorer, a flexible python-based image analysis and visualization tool. Neurophotonics. 2017; 4(3):031210.

Jammalamadaka SR, Sengupta A. Topics in circular statistics, vol. 5. world scientific; 2001.

Karimi Abadchi J, Nazari-Ahangarkolaee M, Gattas S, Bermudez-Contreras E, Luczak A, McNaughton BL, Mohajerani MH. Spatiotemporal patterns of neocortical activity around hippocampal sharp-wave ripples. Elife. 2020 Mar; 9.

Kreuz T, Mulansky M, Bozanic N. SPIKY: A graphical user interface for monitoring spike train synchrony. J Neurophysiol. 2015; 113:3432.

Kreuz T, Satuvuori E, Pofahl M, Mulansky M. Leaders and followers: Quantifying consistency in spatio-temporal propagation patterns. New Journal of Physics. 2017; 19:043028.

Kuznetsova A, Brockhoff PB, Christensen RHB. lmerTest Package: Tests in Linear Mixed Effects Models. Journal of Statistical Software. 2017; 82(13):1–26. doi: 10.18637/jss.v082.i13.

Lein ES, Hawrylycz MJ, Ao N, Ayres M, Bensinger A, Bernard A, Boe AF, Boguski MS, Brockway KS, Byrnes EJ, Chen L, Chen L, Chen TM, Chin MC, Chong J, Crook BE, Czaplinska A, Dang CN, Datta S, Dee NR, et al. Genome-wide atlas of gene expression in the adult mouse brain. Nature. 2007 Jan; 445(7124):168–176.

Makino H, Ren C, Liu H, Kim AN, Kondapaneni N, Liu X, Kuzum D, Komiyama T. Transformation of Cortex-wide Emergent Properties during Motor Learning. Neuron. 2017 May; 94(4):880–890.e8.

Matuschek H, Kliegl R, Vasishth S, Baayen H, Bates D. Balancing Type I error and power in linear mixed models. Journal of Memory and Language. 2017; 94:305–315.

van Meer MPA, van der Marel K, Wang K, Otte WM, El Bouazati S, Roeling TAP, Viergever MA, Berkelbach van der Sprenkel JW, Dijkhuizen RM. Recovery of sensorimotor function after experimental stroke correlates with restoration of resting-state interhemispheric functional connectivity. J Neurosci. 2010 Mar; 30(11):3964–3972.

van Meer MPA, Otte WM, van der Marel K, Nijboer CH, Kavelaars A, van der Sprenkel JWB, Viergever MA, Dijkhuizen RM. Extent of bilateral neuronal network reorganization and functional recovery in relation to stroke severity. J Neurosci. 2012 Mar; 32(13):4495–4507.

bioRxiv preprint doi: https://doi.org/10.1101/2020.07.10.197509; this version posted July 11, 2020. The copyright holder for this preprint (which was not certified by peer review) is the author/funder, who has granted bioRxiv a license to display the preprint in perpetuity. It is made available under a CC-BY-NC-ND 4.0 International license.
Manuscript submitted to eLife

Mitra A, Kraft A, Wright P, Acland B, Snyder AZ, Rosenthal Z, Czerniewski L, Bauer A, Snyder L, Culver J, et al. Spontaneous infra-slow brain activity has unique spatiotemporal dynamics and laminar structure. Neuron. 2018; 98(2):297–305.

Mulansky M, Kreuz T. PySpike - A Python library for analyzing spike train synchrony. Software X. 2016; 5:183.

Pasquini M, Lai S, Spalletti C, Cracchiolo M, Conti S, Panarese A, Caleo M, Micera S. A robotic system for adaptive training and function assessment of forelimb retraction in mice. IEEE Transactions on Neural Systems and Rehabilitation Engineering. 2018; 26(9):1803–1812.

Prabhakaran S, Zarahn E, Riley C, Speizer A, Chong JY, Lazar RM, Marshall RS, Krakauer JW. Inter-individual variability in the capacity for motor recovery after ischemic stroke. Neurorehabilitation and neural repair. 2008; 22(1):64–71.

Quian Quiroga R, Kreuz T, Grassberger P. Event Synchronization: A simple and fast method to measure synchronicity and time delay patterns. Phys Rev E. 2002; 66:041904.

Rehme AK, Volz LJ, Feis DL, Bomilcar-Focke I, Liebig T, Eickhoff SB, Fink GR, Grefkes C. Identifying Neuroimaging Markers of Motor Disability in Acute Stroke by Machine Learning Techniques. Cereb Cortex. 2015 Sep; 25(9):3046–3056.

Satuvuori E, Mulansky M, Bozanic N, Malvestio I, Zeldenrust F, Lenk K, Kreuz T. Measures of spike train synchrony for data with multiple time scales. J Neurosci Methods. 2017; 287:25–38.

Spalletti C, Alia C, Lai S, Panarese A, Conti S, Micera S, Caleo M. Combining robotic training and inactivation of the healthy hemisphere restores pre-stroke motor patterns in mice. eLife. 2017 dec; 6:e28662. doi: 10.7554/eLife.28662.

Spalletti C, Lai S, Mainardi M, Panarese A, Ghionzoli A, Alia C, Gianfranceschi L, Chisari C, Micera S, Caleo M. A robotic system for quantitative assessment and poststroke training of forelimb retraction in mice. Neurorehabilitation and neural repair. 2014; 28(2):188–196.

Steinmetz NA, Zatka-Haas P, Carandini M, Harris KD. Distributed coding of choice, action and engagement across the mouse brain. Nature. 2019; 576(7786):266–273.

Stinear CM, Lang CE, Zeiler S, Byblow WD. Advances and challenges in stroke rehabilitation. Lancet Neurol. 2020 Apr; 19(4):348–360.

Townsend RG, Gong P. Detection and analysis of spatiotemporal patterns in brain activity. PLoS computational biology. 2018; 14(12):e1006643.

Vanni MP, Chan AW, Balbi M, Silasi G, Murphy TH. Mesoscale Mapping of Mouse Cortex Reveals Frequency-Dependent Cycling between Distinct Macroscale Functional Modules. Journal of Neuroscience. 2017; 37(31):7513–7533. https://www.jneurosci.org/content/37/31/7513, doi: 10.1523/JNEUROSCI.3560-16.2017.

Vanni MP, Murphy TH. Mesoscale transcranial spontaneous activity mapping in GCaMP3 transgenic mice reveals extensive reciprocal connections between areas of somatomotor cortex. J Neurosci. 2014 Nov; 34(48):15931–15946.

Yanai H, Takeuchi K, Takane Y. Projection Matrices, Generalized Inverse Matrices, and Singular Value Decomposition. Springer; 2011. doi: 10.1007/978-1-4419-9887-3.

bioRxiv preprint doi: https://doi.org/10.1101/2020.07.10.197509; this version posted July 11, 2020. The copyright holder for this preprint (which was not certified by peer review) is the author/funder, who has granted bioRxiv a license to display the preprint in perpetuity. It is made available under a CC-BY-NC-ND 4.0 International license.
Manuscript submitted to eLife

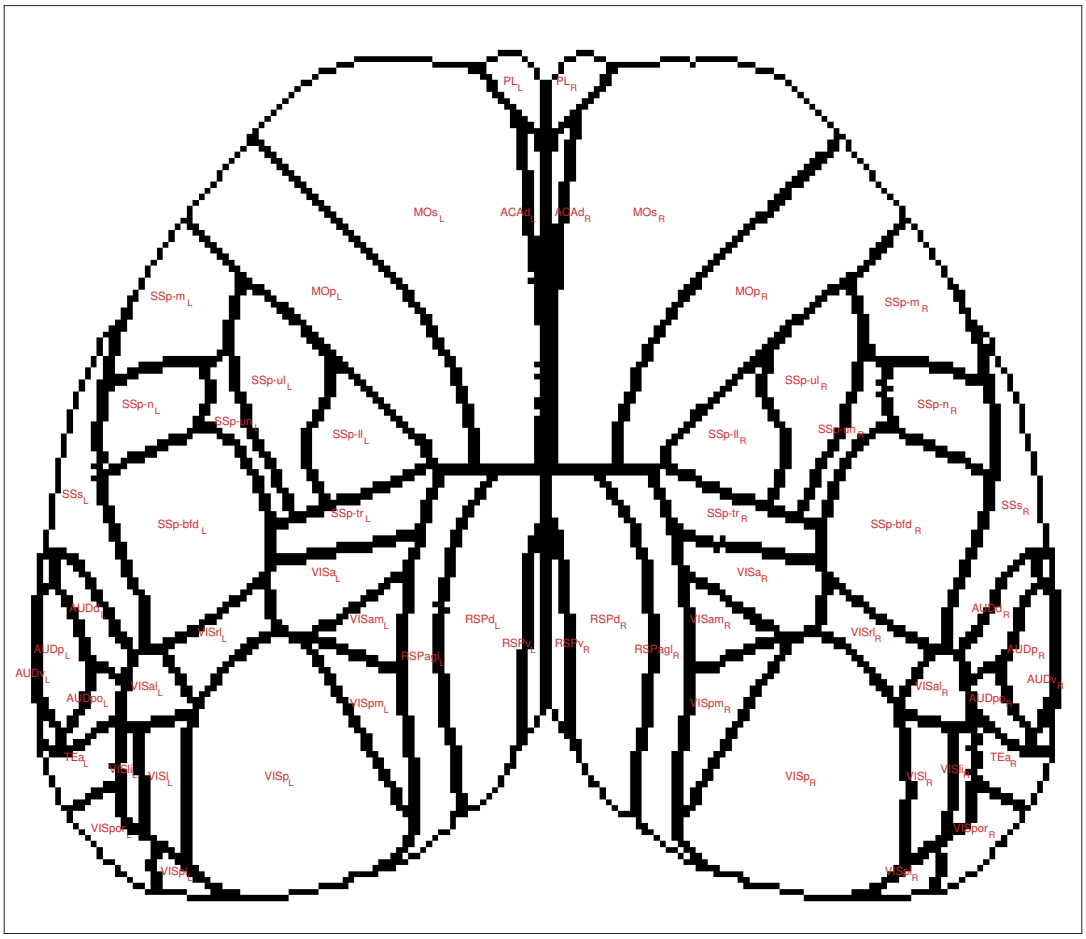

Figure 1–Figure supplement 1. Standard atlas of brain regions.

Acronym	Name	Acronym	Name
MOp	Primary motor area	VISam	Anteromedial visual area
MOs	Secondary motor area	VISl	Lateral visual area
SSp-n	Primary somatosensory area	VISp	Primary visual area
SSp-bfd	Primary somatosensory area	VISpl	Posterolateral visual area
SSp-ll	Primary somatosensory area	VISpm	posteromedial visual area
SSp-m	Primary somatosensory area	VISli	Laterointermediate area
SSp-ul	Primary somatosensory area	VISpor	Postrhinal area
SSp-tr	Primary somatosensory area	ACAd	Anterior cingulate area
SSp-un	Primary somatosensory area	PL	Prelimbic area
SSs	Supplemental somatosensory area	RSPagl	Retrosplenial area
AUDd	Dorsal auditory area	RSPd	Retrosplenial area
AUDp	Primary auditory area	RSPv	Retrosplenial area
AUDpo	Posterior auditory area	VISa	Anterior area
AUDv	Ventral auditory area	VISrl	Rostrolateral visual area
VISal	Anterolateral visual area	TEa	Temporal association areas

Figure 1–Figure supplement 2. Brain regions acronyms.

bioRxiv preprint doi: https://doi.org/10.1101/2020.07.10.197509; this version posted July 11, 2020. The copyright holder for this preprint (which was not certified by peer review) is the author/funder, who has granted bioRxiv a license to display the preprint in perpetuity. It is made available under a CC-BY-NC-ND 4.0 International license.

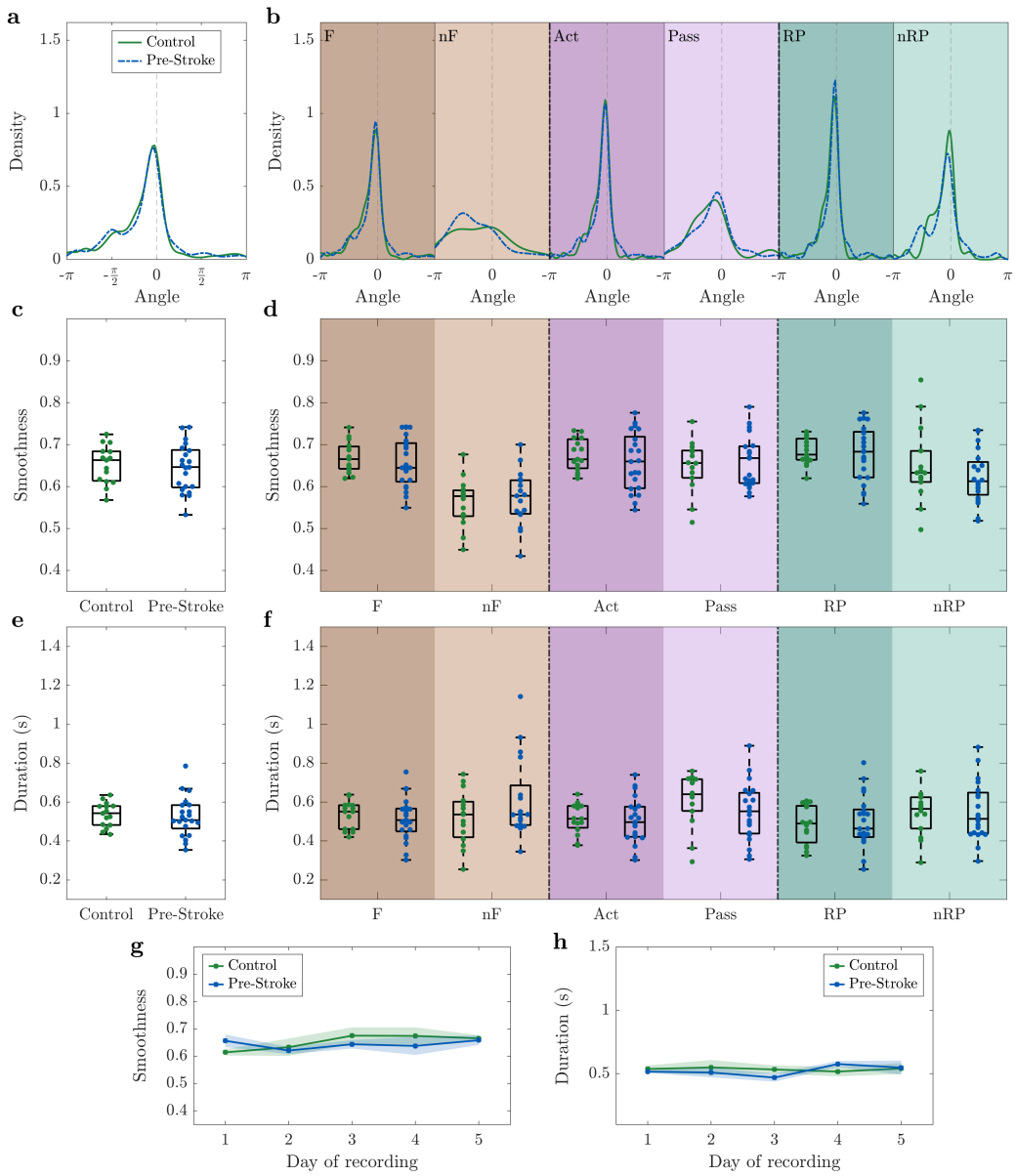

Figure 5–Figure supplement 1. The pre-stroke condition presents the same behaviour as the control group, both qualitatively and quantitatively, for all the investigated spatiotemporal indicators: **(a-b)** angle, **(c-d,g)** smoothness, and **(e-f,h)** duration. — Angle and duration are weighted by smoothness. Markers in (c-h) refer to the average value per day. Within each box in (c-f), the central mark indicates the median, and the bottom and top edges of the box indicate the 25th and 75th percentiles, respectively. Shaded areas in (g-h) correspond to the confidence interval. Control group n=3 mice, pre-stroke group n=5 mice.

bioRxiv preprint doi: https://doi.org/10.1101/2020.07.10.197509; this version posted July 11, 2020. The copyright holder for this preprint (which was not certified by peer review) is the author/funder, who has granted bioRxiv a license to display the preprint in perpetuity. It is made available under a CC-BY-NC-ND 4.0 International license.

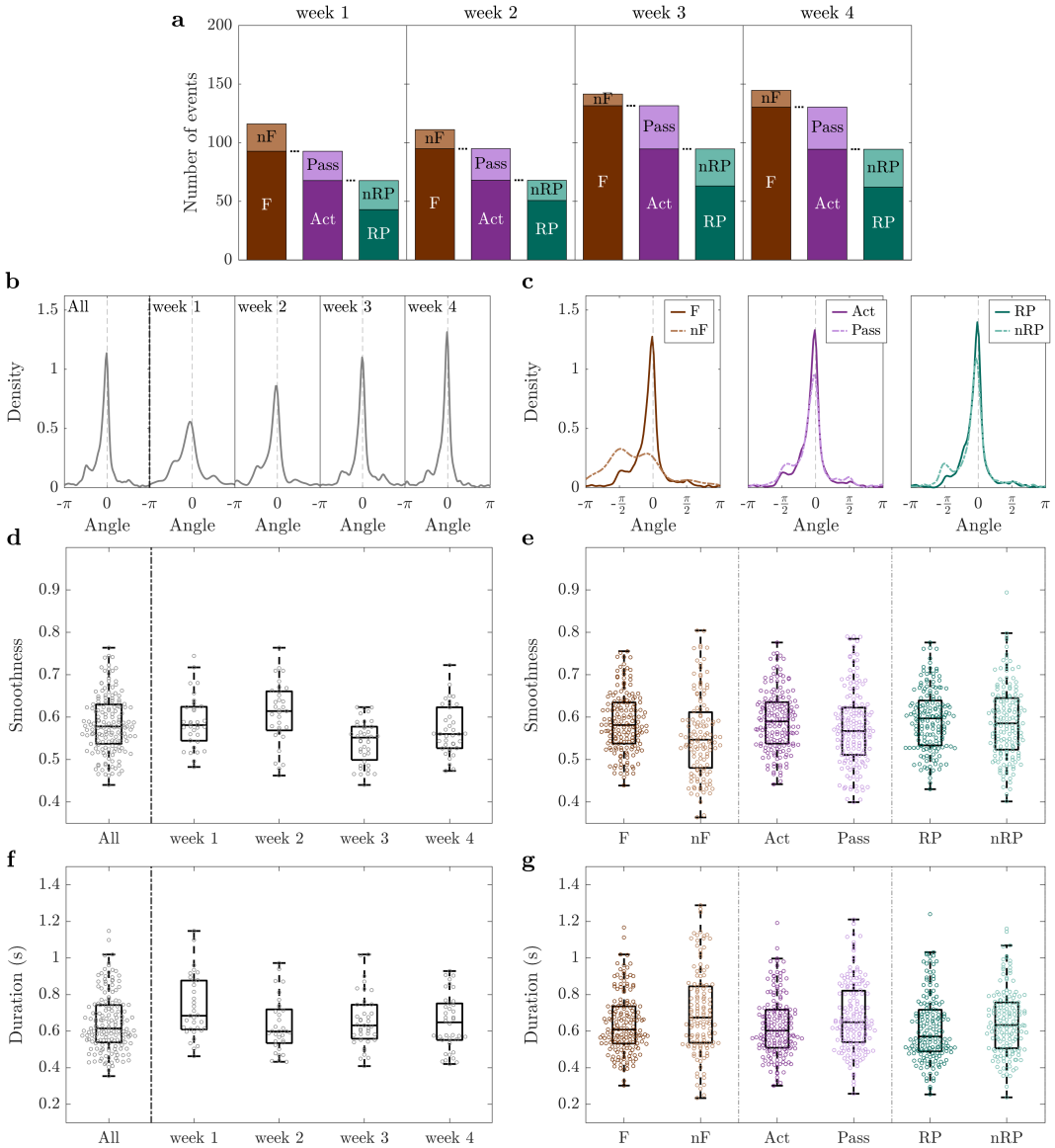

Figure 6–Figure supplement 1. The robot group presents a non-stationary evolution over weeks and large variance of all three indicators. **(a)** Mean number of events for all eight mice per week, partitioned by type of event. **(b)** Motor training rehabilitation causes more and more directed propagation patterns. **(c)** Narrowing down the type of event leads to more directed propagation patterns. **(d-e)** Smoothness does not discriminate event types and oscillates over weeks. **(f-g)** Event duration stabilises starting from the second week of training after stroke. — Angle and duration are weighted by smoothness. Markers in (d-g) refer to the average value per day. Within each box in (d-g), the central mark indicates the median, and the bottom and top edges of the box indicate the 25th and 75th percentiles, respectively. Robot group n=8 mice.

bioRxiv preprint doi: https://doi.org/10.1101/2020.07.10.197509; this version posted July 11, 2020. The copyright holder for this preprint (which was not certified by peer review) is the author/funder, who has granted bioRxiv a license to display the preprint in perpetuity. It is made available under a CC-BY-NC-ND 4.0 International license.

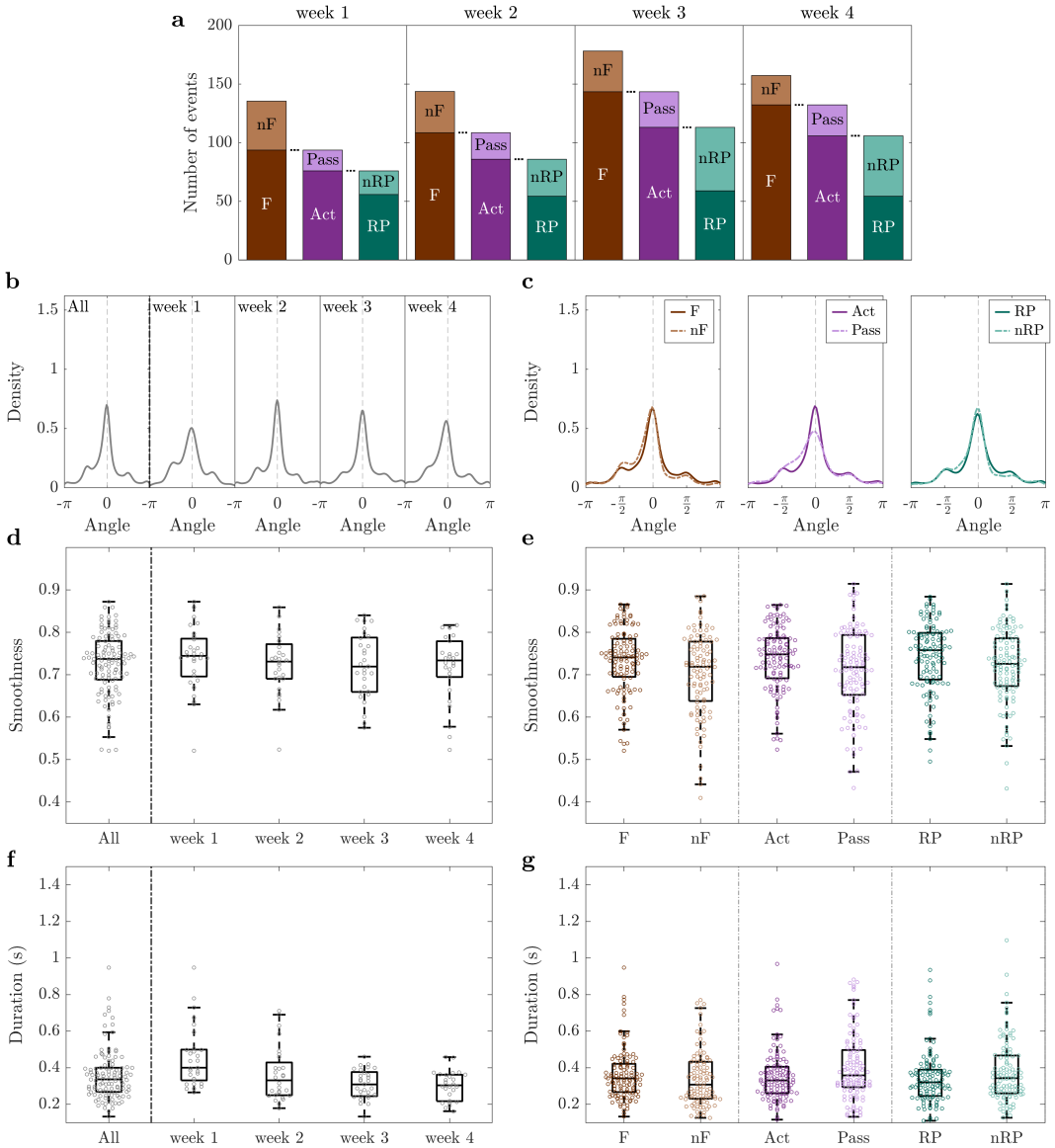

Figure 6–Figure supplement 2. The rehab group shows high coherence of all three spatiotemporal indicators starting from the second week of training after stroke. **(a)** Mean number of events for all six mice per week, partitioned by type of event. **(b-c)** The angle of the propagation is not altered by either motor training or splitting by event types. **(d-e)** Smoothness does not discriminate event types and it is stable over weeks. **(f-g)** Event duration decreases over weeks. — Angle and duration are weighted by smoothness. Markers in (d-g) refer to the average value per day. Within each box in (d-g), the central mark indicates the median, and the bottom and top edges of the box indicate the 25th and 75th percentiles, respectively. Rehab group n=6 mice.